High Performance Single-Phase Single-Stage Grid-Tied PV Current Source Inverter Using Cascaded Harmonic Compensators

Nahla E. Zakzouk [1], Ahmed K. Abdelsalam [1,*], Ahmed A. Helal [1] and Barry W. Williams [2]

[1] Electrical and Control Engineering Department, College of Engineering, Arab Academy for Science and Technology (AAST), Alexandria 1029, Egypt; nahla.zakzouk@aast.edu (N.E.Z.); ahmed.anas@aast.edu (A.A.H.)
[2] Electronics and Electrical Engineering Department, Faculty of Engineering, University of Strathclyde, Glasgow G11XQ, UK; barry.williams@eee.starth.ac.uk
*   Correspondence: ahmed.kadry@aast.edu

Abstract: In this paper, a single-phase single-stage photovoltaic (PV) grid-tied system is investigated. The conventional pulse width modulated (PWM) voltage source inverter (VSI) is replaced by a PWM current source inverter (CSI) for its voltage boosting capabilities, inherent short-circuit proof and higher reliability features. Modeling, design, and analysis of the considered CSI are presented altogether with enhanced proposed control loops aided with a modified PWM technique. DC-link even current harmonics are commonly reflected as low-order odd harmonics in the grid resulting in a poor quality grid current. In order to overcome the latter, a high performance proportional resonant controller, applied in the inverter inner grid current loop, is proposed using cascaded resonant control units tuned at low-order frequencies to eliminate injected grid current harmonics. Hence, with a less-bulky smoothing inductor at the CSI DC-side, grid power quality and system efficiency are simultaneously improved. Simulation and experimental results verify the proposed controller effectiveness.

Keywords: photovoltaic; current source inverter; proportional resonant controller; cascaded harmonic compensator

1. Introduction

World's increasing energy consumption, depleting fossil fuels, and environmental problems encourage the use of renewable energy resources recently. Among the latter, photovoltaic (PV) energy has become a promising resource [1,2]. For best utilization of electric power, grid-connected photovoltaic systems offer high return-on-investment as they supply the maximum extracted PV power into the grid without the need of battery back-ups [3–6].

Commercial PV-grid interface technologies include central, string inverters and AC modules [7,8]. For string inverter topology, a number of PV modules form a string, each having its own inverter, thus maximum power point tracking (MPPT) is separately achieved for each PV string. This overcomes non flexibility, MPPT mismatch, and power losses caused by the old centralized inverter topology. However, the string topology still suffers limited modularity because the whole string is operated at a single maximum power point (MPP). The latter may cause PV modules' mismatch due to manufacturing tolerances or non-optimal conditions such as partial shading [9]. Hence, the "plug and play" user friendly module integrated converter (MIC) concept arises where a single PV module is integrated with an inverter into one unit regarded as a PV AC module connected in parallel to the grid [10]. This

eliminates mismatch losses between PV modules and supports optimal adjustment between the PV module and the inverter. Hence the modular integrated converter topology is considered in this article.

For low-to-medium power applications, energy resources are usually connected to the AC grid through a single-phase voltage source inverter (VSI) at network distribution low voltage level (110/220 V) [11]. Single-and two-stage grid-connected converters are commonly used topologies in single-phase PV applications [7] to achieve functions of PV maximum power tracking and PV-grid interface [12,13]. In the two-stage topology, a power decoupling DC/DC stage is added between the PV source and the DC/AC inverter stage for stepping up the PV voltage and tracking the MPP while the DC/AC inverter interfaces the PV source to the grid. This topology has the merit of decoupling the PV module from the output inverter stage. Hence, the inverter DC-bus voltage ripples, resulting from the known double line-frequency grid power oscillations due to the single-phase connection, would have limited impact on the PV source [14,15]. However, this topology suffers from higher part count, reduced efficiency, lower reliability, higher cost, and larger footprint when compared to its alternative; the single-stage topology [16,17]. The latter involves a single conversion stage (DC/AC power inverter) to achieve PV MPPT altogether with PV-grid interface. Hence, system component count is minimized increasing conversion efficiency, system reliability and meanwhile reducing its size and cost. However, for such a topology, when applying a conventional H-bridge VSI, it must be followed by a step-up transformer to overcome the bucking feature of the VSI which adversely contributes to the increase of the system size, cost, and additional losses. Furthermore, a large electrolytic capacitor must be connected between the PV source and the VSI to limit DC-link voltage ripples' propagation to the PV output power [18,19]. These capacitors are the limiting factor of the inverter lifetime and system reliability.

Since the efficiency and footprint of the two-stage grid-connected system are not appealing, especially for low and medium power applications, single-stage topology is considered in this article. However, to overcome the voltage-buck property of the VSI and the required large electrolytic capacitor at the DC-bus, the VSI can be replaced by a single-phase pulse width modulated current source inverter (PWM CSI) [20–27]. CSIs are highly competitive to VSIs with their integrated voltage boost functionality, ability to produce near sinusoidal low Total Harmonic Distortion (THD) voltage generation and inherent short-circuit protection capability provided by the DC inductor [28]. Hence, it can be a viable alternative for the interconnection of a low-voltage PV array to grid without the need of an additional component for voltage boosting. In summary, PV CSI offers high reliability at relatively high efficiency when compared to that of voltage source based solar inverter [29].

However, the input DC current of the single-phase grid-connected CSI inherently contains even harmonics which affect PV MPPT, reduce the PV panels' lifetime, producing odd-order harmonics on the grid side [21]. Conventionally, to suppress these DC-side harmonics, a large DC inductor is applied, however at the cost of a bulky system realization which is practically inconvenient. Various techniques have been proposed to eliminate CSI DC-side harmonics without the need of large inductor. Hardware solutions are common [26,27]. In [26], an additional doubled-tuned parallel resonant circuit is placed on the DC-link inductor in order to eliminate DC-side second and fourth order harmonics. However, these extra passive elements add to the entire system size, cost, losses and design complexity. In [27], an active buffer, power decoupling circuit, is added between the DC-link inductor and the CSI yet at the cost of more component count and system losses. Hence, software/control technique-based solutions are preferred. Specially-designed feedback current controllers are proposed in [20,21,25] to eliminate the DC-side harmonics without the need of bulky inductor. In [20], pulse amplitude modulation (PAM) is applied where the carrier signal is varied with the DC-link second-order harmonic component to eliminate its effect on the AC grid current. Analog-based active nonlinear pulse width modulation (NPWM) has been proposed in [21] to improve AC-side harmonic mitigation. In [25], the third-order harmonic grid current is mitigated by employing a tuned proportional resonant controller at the harmonic order. However, for all these control solutions, a DC source is assumed as an input rather than an actual PV source.

In this paper, an enhanced performance modified cascaded proportional resonant controller, applied to single phase-single-stage PV grid-connected CSI, is proposed. The proposed controller offers high performance grid integration and MPPT using reduced-size DC-link inductor, thus offering system reduction in both footprint and cost without violating the standard grid code. Modeling, design and analysis of the applied CSI are presented altogether with enhanced performance proposed control loops. Furthermore, the CSI DC inductor value is reduced and meanwhile grid current harmonics are minimized using the proposed cascaded proportional resonant (CPR) controller implemented in the inverter grid current control loop. This controller is associated with harmonic compensator units tuned at low-order grid current harmonics to be selectively eliminated. System performance using reduced value DC-link inductor is investigated when applying a conventional proportional resonant (PR) grid current controller and then retested with the proposed CPR controller. Simulation and experimental results for both cases are compared to verify the effectiveness of the proposed controller on grid current quality.

2. System under Investigation

The investigated topology is a single-phase single-stage grid-connected PV system as shown in Figure 1a. It consists of a full-bridge single-phase CSI. The inverter AC side is connected to 110 V, 50 Hz grid through a *CL* low-pass filter, in the form of L_f and C_f. The inverter input is connected to ASE-285-DGF/17 PV module, with specifications shown in Table 1, through a DC-link inductor L_{dc}.
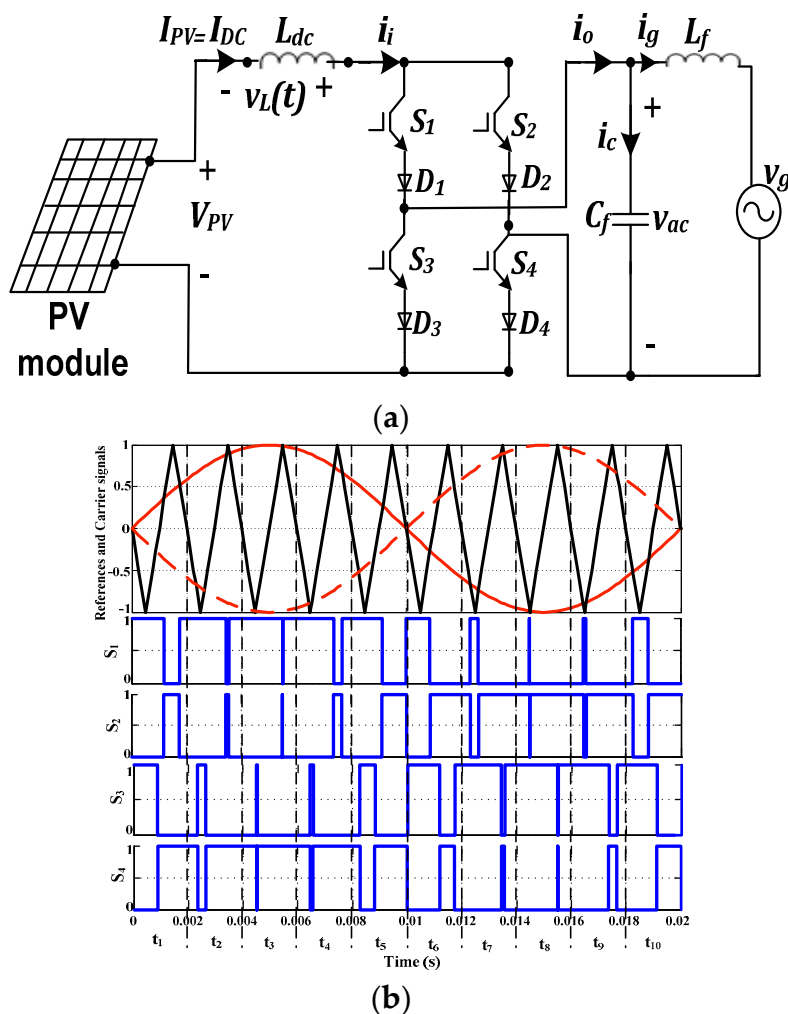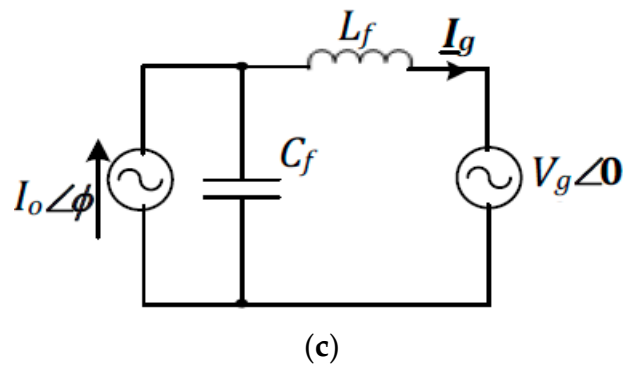

(**a**)

(**b**)

Figure 1. *Cont.*

(c)

Figure 1. PV-grid connected system under investigation. (**a**) System topology, (**b**) modified sinusoidal pulse width modulation (SPWM) gating signals, (**c**) grid connected current source inverter (CSI) equivalent circuit.

Table 1. PV panel (ASE-285-DGF/17) parameters used in simulation analysis.

Nominal short circuit current (I_{SCn})	18.4	A
Nominal open circuit voltage (V_{OCn})	20	V
Maximum power current (I_{MPP})	16.8	A
Maximum power voltage (V_{MPP})	17	V
Maximum output power (P_{max})	285	W
Current/temp. coefficient (K_i)	18.4×10^{-3}	A/°C
Voltage/temp. coefficient (K_v)	-7.6×10^{-2}	V/°C
Series cells	216	-

2.1. Applied Pulse Width Modulation Scheme

Conventional single-phase CSI PWM emerged late 90's [20] and recently enhanced [21,24], depends on sinusoidal pulse width modulation (SPWM). To ensure DC-link current continuity, the upper switches are ON for half the fundamental cycle and the lower switches are sinusoidally modulated [30]. However, this PWM lacks symmetrical utilization of the upper and lower switches, even losses distribution and high carrier frequency usage. Other PWM methods solves this issue using on-line PWM generation technique for single phase CSI's, which is an enhanced version of the three-phase CSI relying on the duality theory [30]. The presented method offers equal distribution of the shoot-through pulses and uniform losses distribution among the inverter's devices, but with more sophisticated implementation.

Common SPWM techniques used for single-phase VSIs feature bipolar and unipolar techniques [31]. Unipolar SPWM doesn't allow a continuous way for DC current in its zero output AC voltage state hence, the CSI DC side is open-circuited. On the contrary, bipolar SPWM ensures DC current continuity when applied for single-phase CSI offering uniform switching distribution [30]. Higher THD is remarked due to the insufficient overlap time. Hence, a modified carrier based SPWM technique, which consists of two carriers and one reference, was proposed in [26]. The proposed switching technique can provide sufficient short-circuit current after every active switching action, thus grid current THD is reduced. Furthermore, equal pulses distribution among CSI switches is achieved yet with simple implementation, hence adopted in the presented article.

However, since TMS320F28335 DSP is applied in the practical implementation, with its inherited PWM block in MATLAB/Simulink library, it will be difficult to apply two carriers as proposed in [26]. Hence, this paper proposes another realization form for the modified SPWM technique where same gating signals, to those produced in [26], are achieved however with one carrier and two references. The SPWM technique form, applied in this paper for single-phase CSI switching, can be presented as follows; Figure 1b shows the carrier and the references waveforms, along with the switching patterns for one reference period (0.02 s). The reference with the solid straight line is responsible for the upper

switches, while the dashed line reference is responsible for the lower switches and is shifted by 180°. The applied PWM operates in two modes, a conductive mode and a null mode, and the switching action of each switch is equally distributed during every fundamental period.

2.2. System Modelling

For a grid-connected PV system using a CSI, the relationship between the PV output voltage and the grid voltage is derived as follows [26];

For a unity power factor,

$$p_g = \hat{V}_g \hat{I}_g sin^2 \omega t = \frac{\hat{V}_g \hat{I}_g}{2}(1 - cos(2\omega t)), \tag{1}$$

where p_g is the instantaneous active power injected to the grid assuming unity power factor, $\hat{V}_g$ is the grid voltage amplitude, $\hat{I}_g$ is the injected grid current amplitude, and ω is the line angular frequency in rad/s.

By neglecting system losses, the PV output power is equal to the average part of the grid power,

$$V_{PV}I_{PV} = \frac{\hat{V}_g \hat{I}_g}{2}, \tag{2}$$

where V_{PV} and I_{PV} are the PV output voltage and current. The grid current is equal to the PV output current multiplied by the inverter modulating amplitude M.

$$\hat{I}_g = MI_{PV}, \tag{3}$$

Substituting (2) into (3), the equation describing the relationship between the PV output voltage and the grid voltage is:

$$V_{PV} = \frac{M\hat{V}_g}{2}, \tag{4}$$

Therefore, in order to interface the PV system to the grid using a CSI, the PV voltage should not exceed half the grid peak voltage.

From Equation (1), the grid power consists of two components; the DC component (i.e., average grid power) and the AC component (i.e., grid power oscillates by double the line frequency). The latter is reflected at the CSI DC side resulting in oscillating power at the CSI DC-link inductor as follows [21],

$$v_L(t)I_{PV} = -\frac{\hat{V}_g \hat{I}_g}{2}cos(2\omega t) = -V_{PV}I_{PV}cos(2\omega t), \tag{5}$$

where $v_L(t)$ is the instantaneous voltage across L_{dc} as shown in Figure 1a.

Then,

$$v_L(t) = -V_{PV}cos(2\omega t) = -\frac{M\hat{V}_g}{2}cos(2\omega t), \tag{6}$$

This will in-turn result in PV current ripples noted as $i_L(t)$,

$$i_L(t) = -\frac{1}{L_{dc}} \int_0^t v_L(t)dt = \frac{M\hat{V}_g}{4\omega L_{dc}}sin(2\omega t), \tag{7}$$

Then,

$$i_i(t) = I_{PV} + i_L(t) = \frac{2P_{PV}}{M\hat{V}_g} + \frac{M\hat{V}_g}{4\omega L_{dc}}sin(2\omega t), \tag{8}$$

where $i_i(t)$ is the instantaneous inverter input current in which second-order harmonics appear. Since the CSI is modulated with a SPWM function $m(t)$, the instantaneous inverter output current is [21],

$$i_0(t) = m(t)i_i(t) = M\sin\omega t\left(\frac{2P_{PV}}{M\hat{V}_g} + \frac{M\hat{V}_g}{4\omega L_{dc}}\sin(2\omega t)\right), \tag{9}$$

$$i_0(t) = \frac{2P_{PV}}{\hat{V}_g}\sin\omega t + \frac{M^2\hat{V}_g}{4\omega L_{dc}}\sin\omega t\,\sin2\omega t, \tag{10}$$

$$i_0(t) = \frac{2P_{PV}}{\hat{V}_g}\sin\omega t + \frac{M^2\hat{V}_g}{8\omega L_{dc}}\cos\omega t - \frac{M^2\hat{V}_g}{8\omega L_{dc}}\cos3\omega t, \tag{11}$$

Hence, a third order harmonic component is introduced to the inverter output current (i_0) due to the second order harmonics in inverter input current (i_i). In order to mitigate the latter, single-phase grid-tied PV CSIs usually feature large inductors at their DC-link.

2.3. Parameters' Design

Design steps of the CL filter placed at the CSI AC side, is presented then the selection criteria of the CSI DC-link inductor are illustrated.

2.3.1. AC Output Filter

The CSI AC side filter attenuates high frequency harmonics that are associated with switching frequency and it sidebands. The CSI near sinusoidal output voltage is achieved due to the inverter output capacitor bank (C_f).

A sinusoidal output current can be realized, when applying the CSI sinusoidal voltage to the grid voltage, through the interface ac inductor (L_f) [28].

For this filter design [21], consider the equivalent circuit of the CSI output to the grid shown in Figure 1c. Assume that the fundamental component of the CSI output current (I_{o1}) is at an angle ϕ with respect to grid voltage. The output phasor grid current $(\underline{I}_g)$ can be calculated using superposition as follows;

First consider the $I_{o1}\angle\phi$ source,

$$\therefore \underline{I}_{g1} = \frac{-\frac{I_{o1}\angle\phi}{\omega C_f}}{\omega L_f - \frac{1}{\omega C_f}}, \tag{12}$$

Then consider the $V_g\angle0°$ source,

$$\underline{I}_{g2} = \frac{V_g\angle90°}{\omega L_f - \frac{1}{\omega C_f}}, \tag{13}$$

$$\therefore \underline{I}_g = \underline{I}_{g1} + \underline{I}_{g2} = \frac{-\frac{I_{o1}\angle\phi}{\omega C_f} + V_g\angle90°}{\omega L_f - \frac{1}{\omega C_f}}, \tag{14}$$

To achieve unity power factor, then the imaginary part of $\underline{I}_g$ should be equal to zero. Hence,

$$-\frac{I_{o1}\sin\phi}{\omega C_f} + V_g = 0, \tag{15}$$

Then,

$$\sin\phi = \frac{V_g\omega C_f}{I_{o1}}, \tag{16}$$

$$I_g = \frac{I_{o1}}{1 - \omega^2 L_f C_f}\cos\phi, \tag{17}$$

where I_{o1}, V_g, and I_g are the rms values of the CSI fundamental output current, grid voltage and grid current respectively.

From Equation (16), it can be concluded that,

$$cos^2\phi = 1 - \frac{V_g^2\omega^2C_f^2}{I_{o1}^2}, \tag{18}$$

Moreover, the AC output filter is designed so that $I_g = I_{o1}$, then from Equation (17)

$$cos\phi = 1 - \omega^2L_fC_f, \tag{19}$$

Hence, from Equations (18) and (19)

$$\left(1 - \omega^2L_fC_f\right)^2 = 1 - \frac{V_g^2\omega^2C_f^2}{I_{o1}^2} = 1 - \frac{V_g^4\omega^2C_f^2}{P_{PV}^2}, \tag{20}$$

The AC filter is designed so that the inductor reactance is x times the capacitor impedance at the CSI switching frequency fs, then,

$$\omega_sL_f = x\frac{1}{\omega_sC_f} \Rightarrow L_f = x\frac{1}{\omega_s^2C_f}, \tag{21}$$

where $\omega_s = 2\pi f_s$, by substituting (21) into (20),

$$C_f = \frac{P_{PV}}{V_g^2\omega}\sqrt{\frac{x\omega^2}{\omega_s^2}\left(2 - \frac{x\omega^2}{\omega_s^2}\right)}, \tag{22}$$

Using Equations (21) and (22), L_f and C_f are designed based on the selected values of x and ω_s [21].

2.3.2. DC-Link Inductor

The CSI DC link inductor is implemented to mitigate low-order harmonics introduced by the grid at the DC-link. Moreover, it provides a steady DC current to the inverter. It is sized to keep the DC current fluctuations within specified limits in the same way the DC-link capacitor is designed in case of VSI to keep the DC voltage ripples within specified margins [32].

Consider energy balance concept at CSI DC-link, neglecting inverter and filter losses.

$$E_{PV} = E_L + E_g \Rightarrow E_L = E_{PV} - E_g, \tag{23}$$

where E_{PV}, E_L, and E_g are the PV output energy, energy stored in DC-link inductor and grid energy respectively. From Equation (23),

$$\frac{1}{2}L_{dc}\left(I_{dcmax}^2 - I_{dcmin}^2\right) = \int_{\frac{-T}{4}}^{\frac{T}{4}}\left(P_{PV} - p_g\right)dt, \tag{24}$$

where I_{dcmax} and I_{dcmin} are the maximum and minimum values of the average DC-link current respectively. From Equation (1), p_g equals $P_g(1 - cos(2\omega t))$ where P_g is the mean grid power. Assuming loss-less operation, let $P_{PV} = P_g$,

$$\therefore \frac{1}{2}L_{dc}\left(I_{dcmax} + I_{dcmin}\right)\left(I_{dcmax} - I_{dcmin}\right) = \int_{\frac{-2\pi}{4}}^{\frac{2\pi}{4}}P_gcos(2\omega t)d\omega t, \tag{25}$$

$$\therefore\ L_{dc}I_{dc}\Delta i_{dcp-p} = \frac{P_g}{2\omega} \int_{\frac{-2\pi}{4}}^{\frac{2\pi}{4}} \cos(2\omega t)d(2\omega t)\ , \tag{26}$$

where Δi_{dcp-p} is the peak to peak DC current ripple. Let 2ωt = θ,

$$\therefore\ L_{dc}I_{dc}\Delta i_{dcp-p} = \frac{P_g}{2\omega} \int_{-\frac{\pi}{2}}^{\frac{\pi}{2}} \cos\theta\ d\theta, \tag{27}$$

The DC-link inductor that limits DC-current ripple to a desired value can be calculated from Equation (27) resulting in Equation (28) [23],

$$L_{dc} = \frac{P_g}{\omega I_{dc}\Delta i_{dcp-p}} = \frac{P_{PV}}{2\omega I_{dc}\Delta i_{dc}}, \tag{28}$$

where Δi_{dc} is the amplitude of the DC current ripple.

Hence, the considered system parameters are designed according to the previous equations and their values are shown in Table 2 as follows;

Table 2. Investigated system parameters.

L_{dc}	150 mH, for Δi_{dcp-p} = 0.33 A, and 50 mH, for Δi_{dcp-p} = 1 A
C_f, L_f	25 μF and 5 mH for *fs* = 15 kHz

3. Proposed Control Scheme

This section may be divided by subheadings. It should provide a concise and precise description of the experimental results, their interpretation as well as the experimental conclusions that can be drawn.

The proposed control scheme, which achieves single-stage PV-grid interface via single-phase CSI, is demonstrated as follows with design steps summarized in Appendix A;

3.1. CSI Control Loops

CSI features two control loops: an outer DC-link current loop, which regulates the DC-link current to a value that ensures MPPT, and an inner grid current loop for PV-grid interfacing. Figure 2a shows the proposed control scheme.

3.2. Outer DC-Link Current Control Loop

This loop is responsible for forcing the CSI DC-link current I_{dc} (i.e., the PV current IPV) to match a reference value (I_{dcref}). This reference corresponds to the PV current at which the PV module supplies its maximum power (IMPP). Hence, I_{dcref} is determined by an MPPT algorithm in order to extract the PV module maximum power [32]. Several MPPT techniques are discussed in literature [33,34] where variable-step incremental conductance (IncCond.) technique is of main concern due to its simple implementation, high accuracy and less mathematical burden [35–37]. Modified variable step-size IncCond. technique is applied for more enhanced performance [38].
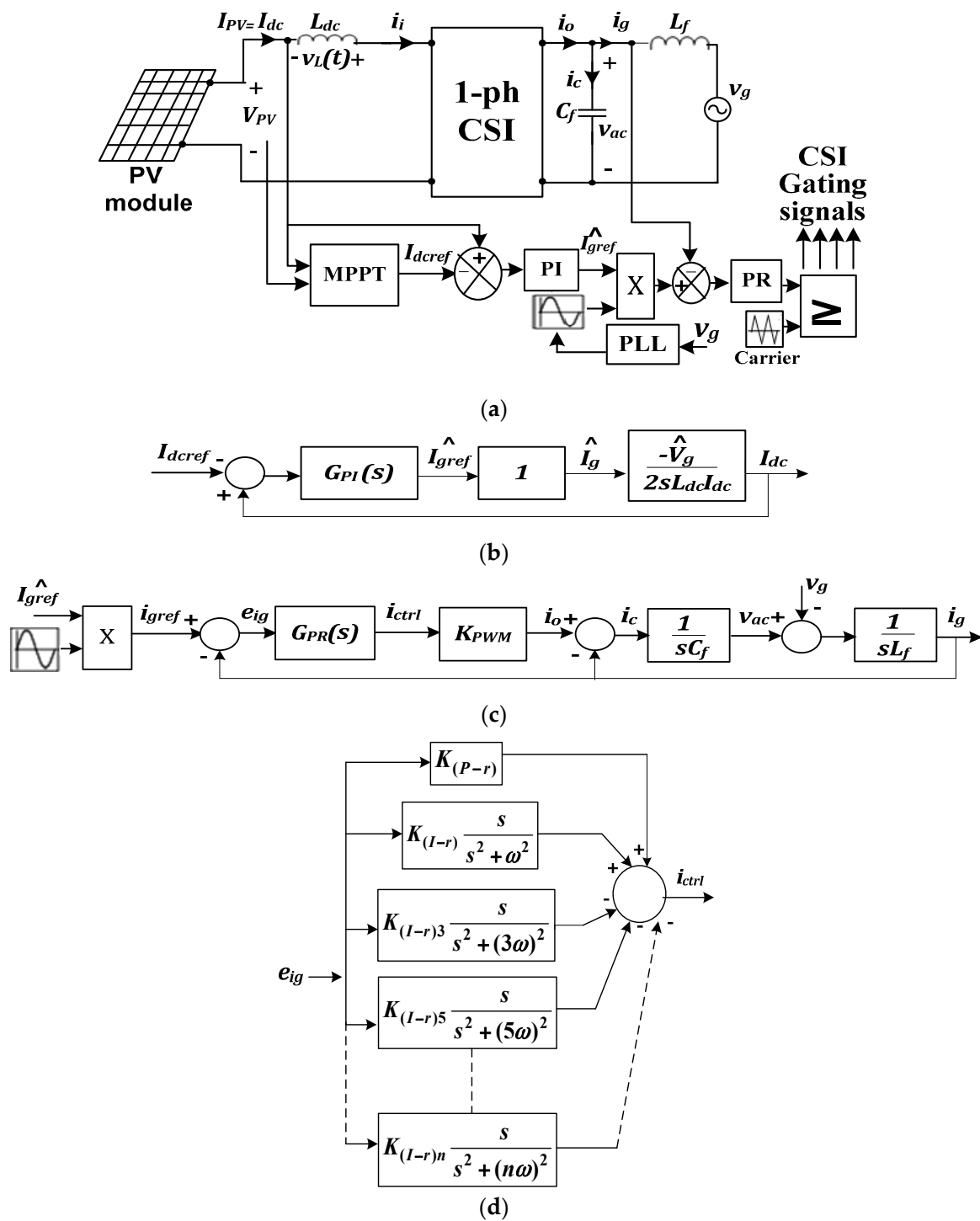
Figure 2. Control scheme for the proposed single-phase single-stage photovoltaic (PV) CSI system: (**a**) schematic diagram, (**b**) outer DC-link control loop, (**c**) inner grid current loop, and (**d**) proposed cascaded harmonic cancellation.

The extracted PV power should be transferred to the grid; hence the output of this loop determines the amplitude of the sinusoidal reference grid current $\hat{I}_{gref}$ insuring the power at the inverter DC-side is transferred to grid [32].

The block diagram of the outer DC-link current control loop is shown in Figure 2b featuring a simple proportional-integral (PI) controller to minimize the DC-link current steady-state error. This controller is represented by the gain GPI(s) where K_{P-i} and K_{I-i} are the controller proportional and integral gains respectively:

$$G_{PI}(s) = K_{P-i} + \frac{K_{I-i}}{s}, \tag{29}$$

The DC-link current controller gains are tuned for a low cross-over frequency to mitigate the magnitude of the double line-frequency DC current oscillations. The inner grid current control loop, with limited bandwidth, can be modeled by a unity gain at the low frequency range as illustrated in Figure 2b [32].

The relationship between variations in the fundamental grid current magnitude and the average DC-link current can be calculated using the average power balance Equation (30), neglecting converter and filter losses:

$$P_{PV} = P_g + \frac{dE_L}{dt}, \tag{30}$$

$$P_{PV} = P_g + \frac{d\left[\frac{1}{2}L_{dc}I_{dc}{}^2\right]}{dt}, \tag{31}$$

In order to carry sensitivity analysis, when studying relationship and correlation between certain system variables, other variables of less contribution can be partially discarded [32]. Consequently, to assess the influence of the grid current on the average DC-link current, one neglects P_{PV} [39]:

$$\frac{d\left[\frac{1}{2}L_{dc}I_{dc}{}^2\right]}{dt} = -P_g, \tag{32}$$

$$\frac{d\left[\frac{1}{2}L_{dc}I_{dc}{}^2\right]}{dt} = -\frac{\hat{V}_g\hat{I}_g}{2}, \tag{33}$$

Applying small perturbations around the operating point:

$$\frac{d\left[\frac{1}{2}L_{dc}(I_{dc} + i_{dc-pert})^2\right]}{dt} = -\frac{\hat{V}_g(\hat{I}_g + \hat{i}_{g-pert})}{2}, \tag{34}$$

where $i_{dc-pert}$, and $\hat{i}_{g-pert}$ are the small perturbations applied around the mean DC-link current and the grid current amplitude respectively. Neglecting steady-state values and square of small perturbations [32]:

$$\frac{d\left[\frac{1}{2}L_{dc}2\,I_{dc}\,i_{dc-pert}\right]}{dt} = -\frac{\hat{V}_g\hat{i}_{g-pert}}{2}, \tag{35}$$

Hence, taking Laplace transform for both sides if Equation (35)

$$L_{dc}I_{dc}sI_{dc}(s) = -\frac{\hat{V}_g\hat{I}_g(s)}{2}, \tag{36}$$

$$\therefore \frac{I_{dc}(s)}{\hat{I}_g(s)} = -\frac{\hat{V}_g}{2sL_{dc}I_{dc}}, \tag{37}$$

3.3. Inner Grid Current Control Loop

For grid integration purposes, the inverter grid current must be of low THD and near-unity power factor. Consequently, the DC current controller output signal is the reference grid current amplitude multiplied by a sinusoidal unit vector, deducted from a phase-locked loop (PLL). The current controller ensures the grid current and its sinusoidal reference matching. The block diagram of the inner grid current control loop is shown in Figure 2c. For high switching frequency, the PWM module can be modeled by a simple gain [39,40]:

$$K_{PWM} = \frac{I_{dc}}{\hat{Tri}},\qquad(38)$$

where $\hat{Tri}$ is the amplitude of the triangular carrier signal.

Since the grid current is time-varying control variable, conventional PI controllers encounter difficulties in removing the steady-state error [41,42]. Hence, either proportional-integral (PI) controllers with feed-forward or proportional-resonant (PR) controllers should be employed [12]. The latter have gained a large popularity in the last decade due to its capability of eliminating the magnitude and phase angle steady-state errors when regulating sinusoidal signals without the need of voltage feed forward [43,44]. Hence, the proportional resonant controller is employed for current control of grid-connected PV VSIs [45] as well as CSIs [26] with the ideal transfer function given as,

$$G_{PR}(s) = K_{P-r} + K_{I-r}\frac{s}{s^2 + \omega^2},\qquad(39)$$

where K_{P-r} is proportional part gain, K_{I-r} is the resonant part gain and ω is the resonant frequency of the controller.

For utilities with wide frequency variations, non-ideal PR controllers [46–48] or damped resonant controllers [49,50] can be used to give a wider bandwidth around the resonant frequency.

Since the fundamental PR controller acts on a very narrow band around its resonant frequency ω, the implementation of harmonic compensator for low-order harmonics is possible without affecting the PR controller behavior and dynamics [51,52]. In addition, single frequency compensation, selective harmonic compensation is proposed by cascading several resonant blocks tuned to resonate at the desired low-order harmonic frequencies to be compensated. Thus, the controller can be suitable for grid-tied systems minimizing its grid current low-order harmonics which result from DC-link even harmonics [21]. The transfer function of the harmonic compensator is given by

$$G_{HC}(s) = \sum_{H = 3, 5, \ldots, n} K_{(I-r)H}\frac{s}{s^2 + (\omega H)^2},\qquad(40)$$

where H is the harmonic order to be compensated for and $K_{(I-r)H}$ represents the individual resonant gain, which must be tuned for minimizing harmonics at the relative frequency.

Ideal PR controllers with harmonic compensators are common with VSIs [45,53–55], however it's not widely used with CSI. In this paper, a harmonic compensator is designed to cancel low-order harmonics as they are the most prominent harmonics in a typical CSI output current spectrum. This allows the use of lower DC-link inductance without degrading grid current quality. The block diagram of the proposed controller is shown in Figure 2d. $K_{(I-r)n}$ is the resonant gain at n^{th} harmonic order designed to limit grid current harmonics at its related frequency.

4. Simulation Results

The investigated single-phase single-stage grid-tied PV system, presented in Section 2, is simulated using MATLAB/Simulink with parameters listed in Appendix C. First, system performance was studied for CSI DC-link inductor (L_{dc}) = 150 mH when applying a conventional PR controller (CPRC) in the grid current loop. Then, L_{dc} was reduced to 50 mH and the latter was repeated once when applying conventional PR controller and again when applying the proposed cascaded harmonic compensator (PCHC). In this paper, a step-change in irradiance; from 1000 W/m^2 to 700 W/m^2 was applied at t = 3 s to study system performance at different power levels in addition to transient investigation.

The system response for the three investigated cases is illustrated in Figure 3. The DC-link current, PV power and average grid power results are shown in Figure 3a–c respectively. The large DC-link inductor, 150 mH case, experienced minimal PV power ripple which was reflected in the grid current THD. At operation start, settling time (t_s) = 0.185 s while at the irradiance step change, the PV maximum power was tracked after 0.025 s. The large size DC-link inductor showed relatively slower tracking response compared to that with 50 mH L_{dc} as will be demonstrated later. System performances for L_{dc} = 50 mH using CPRC and PCHC are shown in Figure 3 as well. Reducing the DC-link inductor to its one third resulted in higher steady-state PV power oscillation which resulted in less average PV power than for L_{dc} = 150 mH case. However, lower losses were experienced by L_{dc} = 50 mH resulting in enhanced system efficiencies of 92%, and 94% at 1000 and 700 W/m^2 respectively in case of CPRC as well as in the case of PCHC. This resulted in more average power delivered at the grid than in case of L_{dc} = 150 mH. Moreover, reducing L_{dc} resulted in a faster dynamic response when applying both controllers (At operation start, t_s = 0.055 s while at the irradiance step change, the PV maximum power was tracked after 0.015 s).

Figure 4 zooms into system response where Figure 4a–f show the effect of the CSI C_f in achieving almost sinusoidal inverter output voltage at 1000 and 700 W/m^2 respectively. Near unity power factor at both irradiance levels for the investigated three cases was fulfilled. The exerted grid currents with their associated fast Fourier analysis (FFT) at both power levels were clarified as well. The high value of L_{dc} resulted in grid current THDs of 4.22% and 4.9% at 1000 and 700 W/m^2 respectively; within IEEE Std. 519 as shown in Figure 4a,d respectively. However, the higher PV power oscillation, in case of L_{dc} = 50 mH, resulted in distorted grid current when applying conventional PR control as shown in Figure 4b,e with THDs beyond standards [56] (9.4% and 12.57% at 1000 and 700 W/m^2 respectively). When studying FFT analysis in case of CPRC, the main cause of high grid current THD was the third order harmonic component (8.9% and 12.25% at 1000 and 700 W/m^2 respectively). Hence, the proposed PR controller was designed with a cascaded harmonic compensator tuned at the third harmonic order to minimize harmonics at this frequency (150 Hz). The impact of the PCHC is shown in Figure 4c,f where grid current third order harmonics were reduced to 1.83% and 2.33% at 1000 and 700 W/m^2 respectively which resulted in a minimized grid current THD (3.19% and 3.93% at 1000 and 700 W/m^2 respectively) which was even better than with L_{dc} = 150 mH. Table 3 summarizes the simulated systems' performance parameters for all cases.

Simulation results show that more PV power oscillation is experienced, when reducing the DC-link inductor, but overall system efficiency and dynamic performance are enhanced. However, a harmonic compensator must be used in the inner grid current control loop to mitigate low-order harmonics found in grid current as a result of higher PV power ripple. Detailed comments on system efficiency are illustrated in the discussion section.
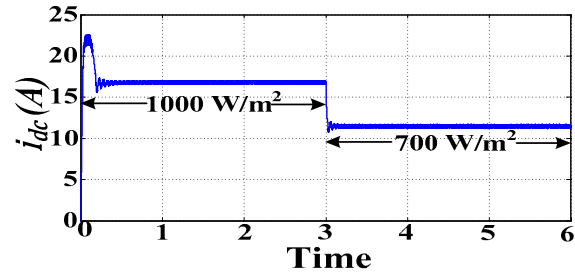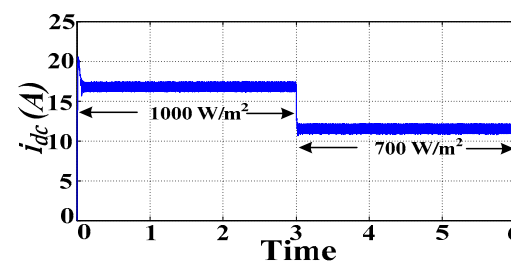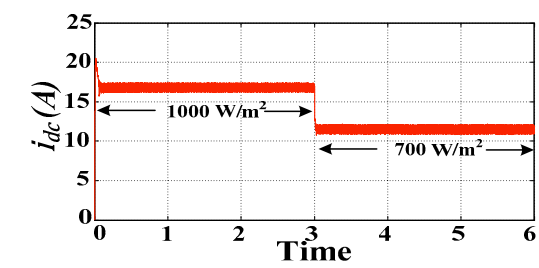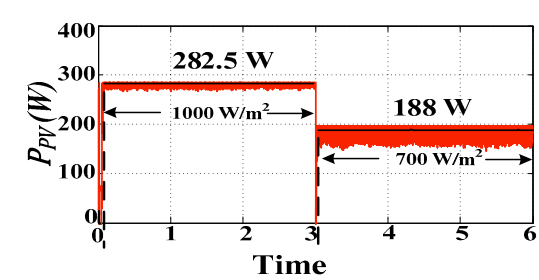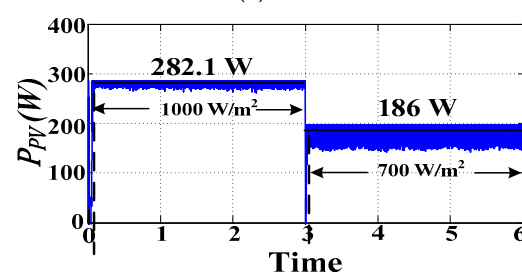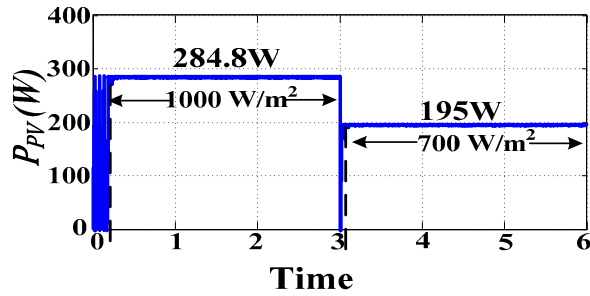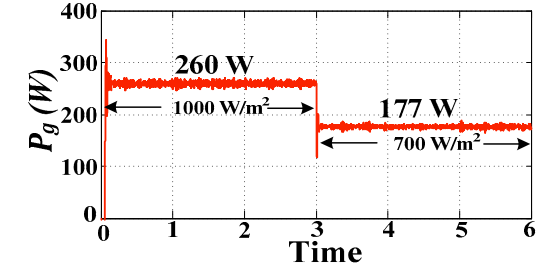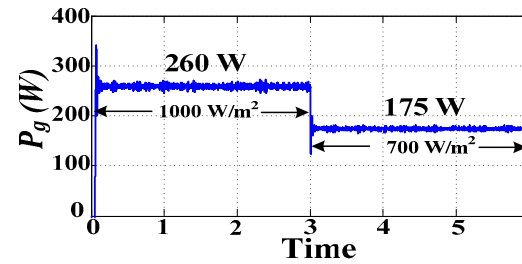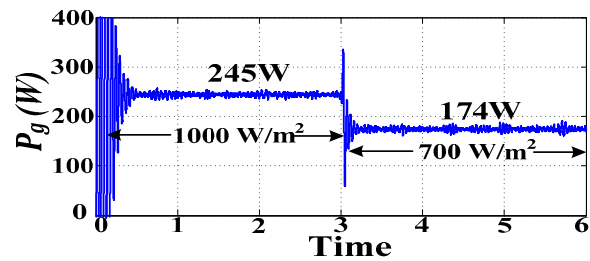
Figure 3. System performance comparison between conventional proportional resonant controller (CPRC) and proposed cascaded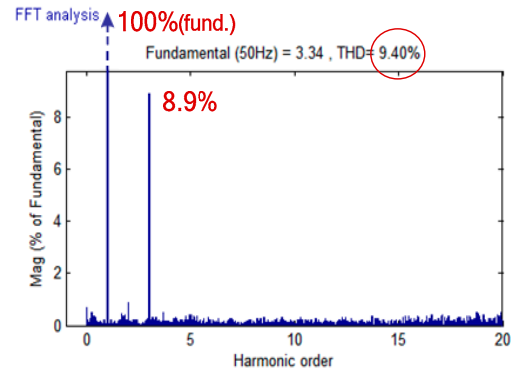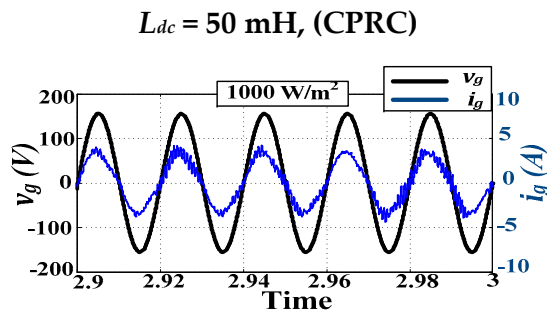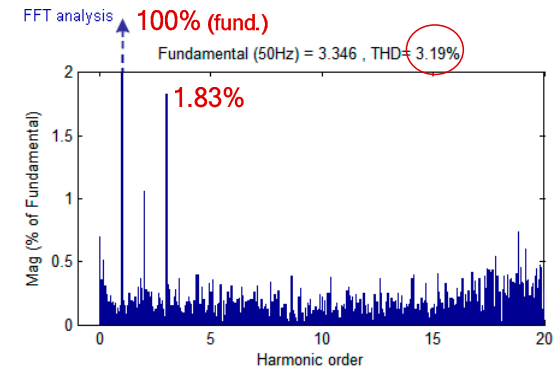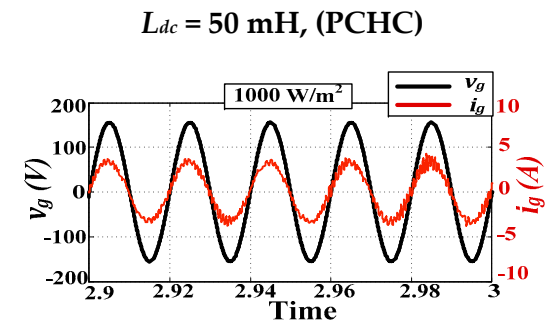 harmonic controller (PCHC) under irradiance variation: (**a**) DC-link current, (**b**) PV power, and (**c**) average grid power.
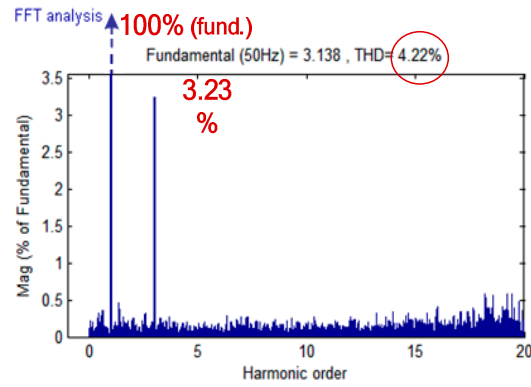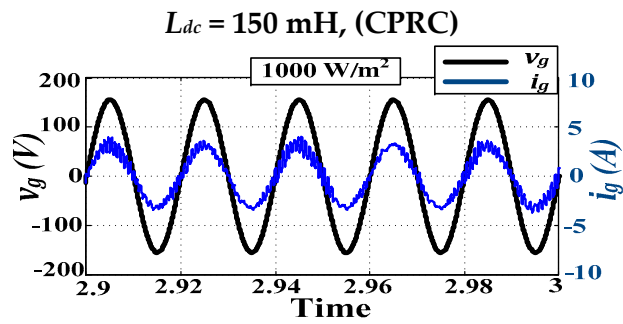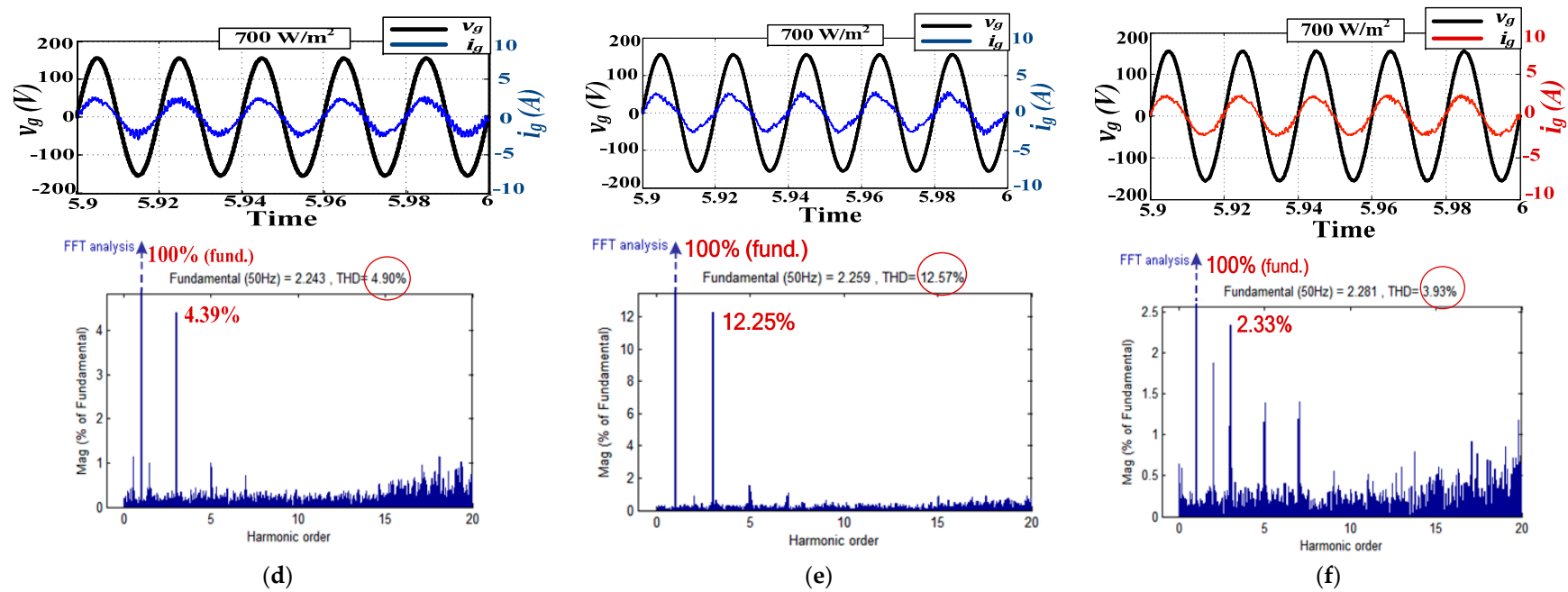
Figure 4. *Cont.*

Figure 4. Zoom on system performance comparison between CPRC and PCHC under irradiance variation: (**a**)–(**c**) high power level, (**d**)–(**f**) low power level.

Table 3. Performance parameters of system applied in simulation work.

Case	Irradiance	Settling Time, (s)	PV Power, (W)	Grid Power, (W)	Overall Efficiency
L_{dc} = 150 mH CPRC	1000 W/m^2	0.185	284.8	245	86%
	700 W/m^2	0.025	195	174	89%
L_{dc} = 50 mH CPRC	1000 W/m^2	0.055	282	260	92%
	700 W/m^2	0.015	186	175	94%
L_{dc} = 50 mH PCHC	1000 W/m^2	0.055	282.5	260	92%
	700 W/m^2	0.015	188	177	94%

5. Experimental Results

The effectiveness of the proposed cascaded harmonic compensator (PCHC), associated with a single-phase single-stage grid-tied CSI, was verified experimentally when co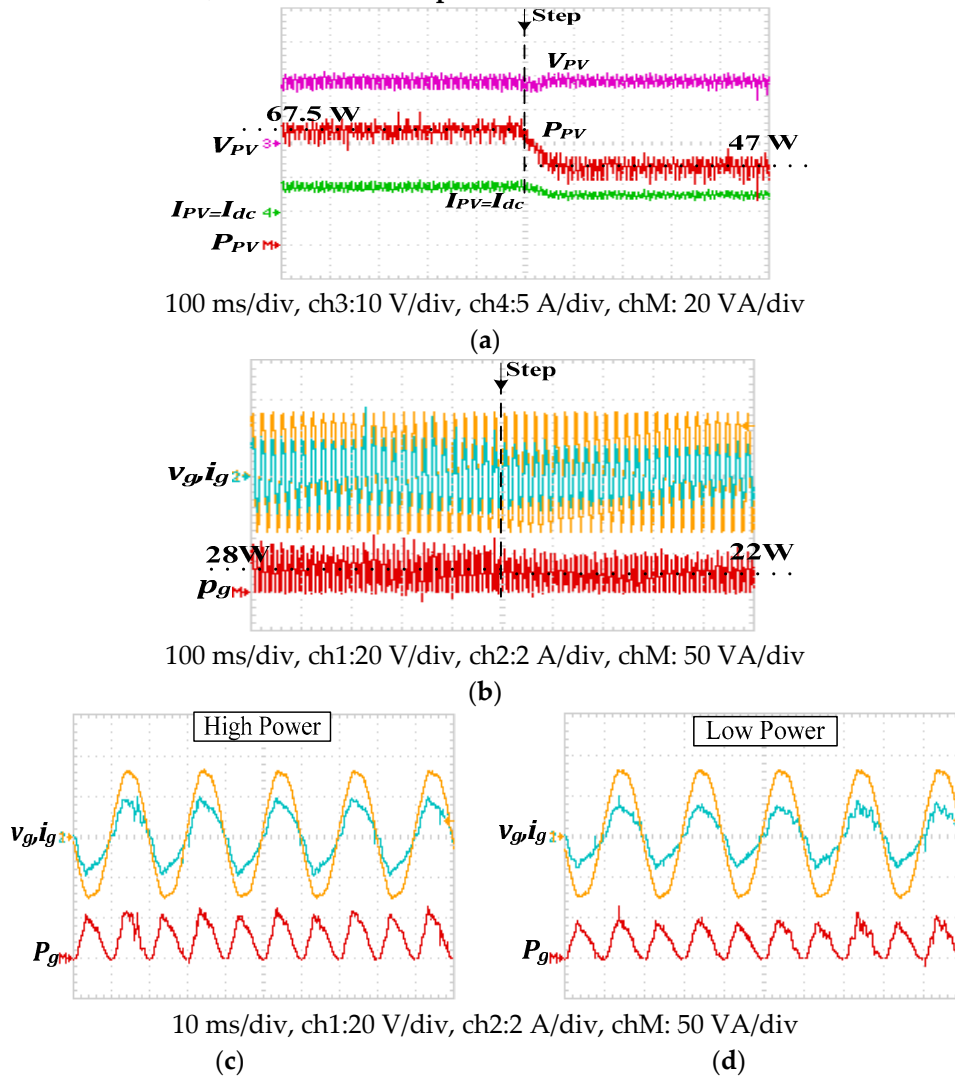mpared to the CPRC performance. However, to hold a valid practical comparison, it is mandatory for both controllers to be tested under similar conditions as listed in Appendix C. Hence, a low-cost simulating circuit [57] was used to emulate PV system operation with the schematic diagram shown in Figure 5a and the Voltage-Current-Power 3-D (V-I-P) curve shown in Figure 5b. A PWM modulated CSI, with f_s of 15 kHz, was connected to the PV emulator output to boost the output voltage, track the maximum power point, and interface the PV system to the grid. A single-phase autotransformer was utilized to emulate the power grid while a TMS320F28335 DSP, featuring a 33-MHz clock, high-speed 12-bit A/D conversion, and 32-bit floating point, was used to generate the PWM signals and realize the proposed feedback loop controllers. The test rig photograph is shown in Figure 5c.

(**a**)

(**b**)　　　　　　　　　　　　　　　　　　　　　　(**c**)
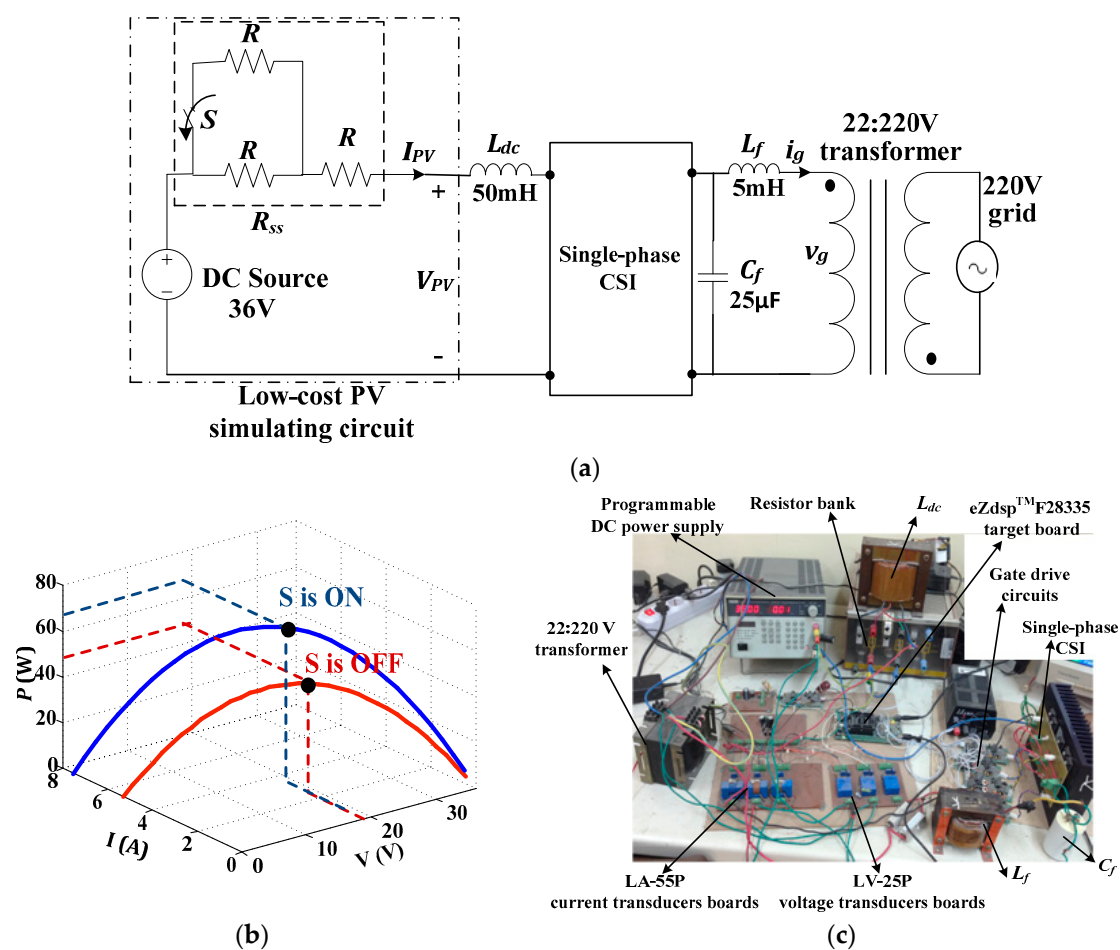
Figure 5. Experimental setup (**a**) schematic diagram, (**b**) P-V, I-V curves of PV emulator under two power levels (**c**) test rig photography.

Both the proposed and the conventional PR controllers were tested for L_{dc} = 50 mH under a step decrease in the PV simulator power (from 67.5 W to 47 W) by opening the switch 'S'. Figure 6a,b show voltage, current and power at the CSI DC side and grid side respectively in case of CPRC while Figure 7a,b show those of PCHC. Both controllers allow the CSI to successfully track the PV maximum power at both power levels and both have the same conversion efficiency. In addition, Figures 6 and 7 zoom into system response when applying CPRC and PCHC respectively. Figure 6c,d show the near unity power factor achieved at both power levels in case of CPRC while Figure 7c,d show those in case of PCHC.

L_{dc} = 50 mH, Conventional Proportional Resonant Controller (CPRC)

100 ms/div, ch3:10 V/div, ch4:5 A/div, chM: 20 VA/div

(**a**)

100 ms/div, ch1:20 V/div, ch2:2 A/div, chM: 50 VA/div

(**b**)

10 ms/div, ch1:20 V/div, ch2:2 A/div, chM: 50 VA/div

(**c**)　　　　　　　　　　　　　　　　　　　　　　(**d**)

Figure 6. System performance applying CPRC, grid voltage THD = 3.9% (**a**) PV voltage, current and power, (**b**) Grid voltage, current and power, (**c**,**d**) zoom of Grid voltage, current and power at high and low power levels respectively.

L_{dc} = 50 mH, Proposed CascadedHarmonic Compensator (PCHC)

100 ms/div, ch3:10 V/div, ch4:5 A/div, chM: 20 VA/div

(**a**)

Figure 7. *Cont.*

100 ms/div, ch1:20 V/div, ch2:2 A/div, chM: 50 VA/div

(**b**)

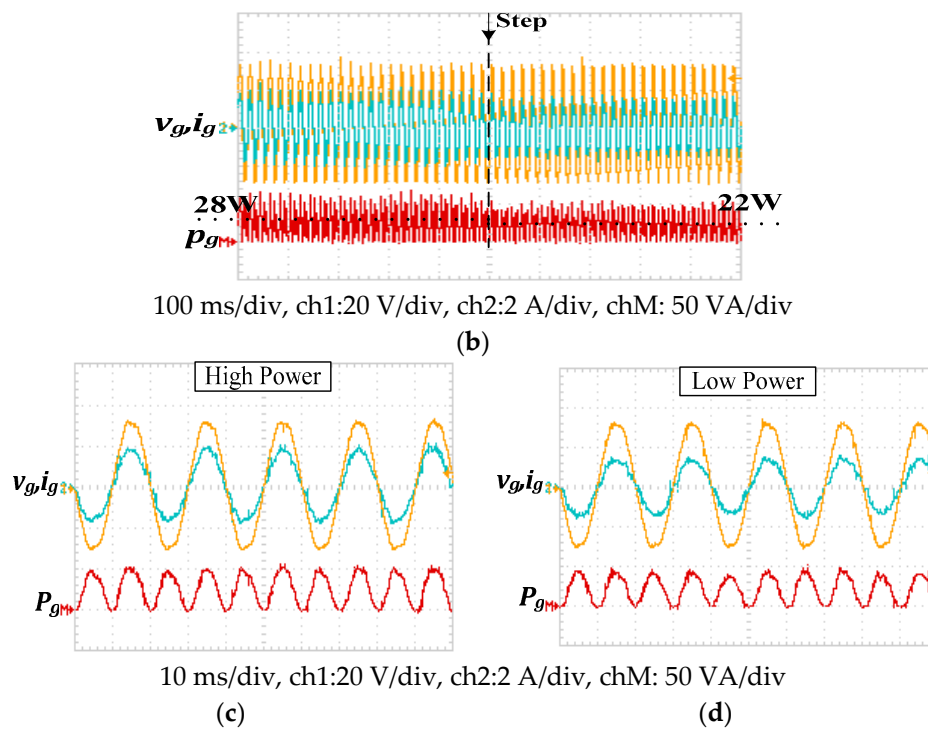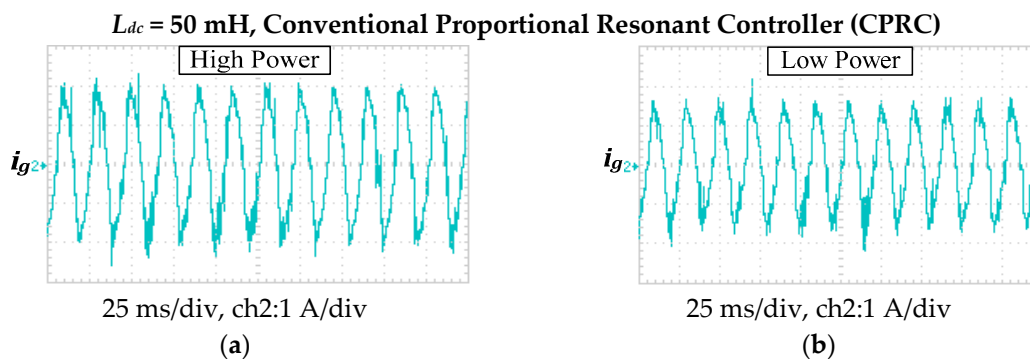10 ms/div, ch1:20 V/div, ch2:2 A/div, chM: 50 VA/div

(**c**) (**d**)
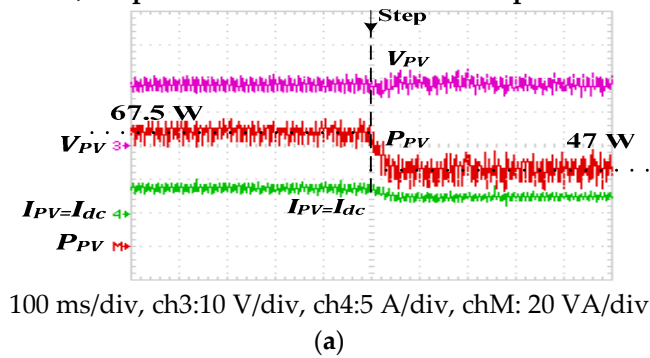
Figure 7. System performance applying PCHC, grid voltage THD = 3.9%. (**a**) PV voltage, current and power, (**b**) Grid voltage, current and power, (**c**,**d**) zoom of Grid voltage, current and power at high and low power levels respectively.

However, Figure 8a–d show the distorted grid current experienced by the conventional PR control with THD beyond IEEE 519 standards (12.26% and 12.97% at higher and lower power levels respectively). When studying grid current FFT analysis in case of CPRC, the third and fifth order components were the most dominant harmonics in grid current waveform spectrum (10.7% and 4% at higher power level and 11.3% and 5% at lower level for the third and fifth harmonics respectively). Hence, a PR controller was designed with a proposed cascaded harmonic compensator tuned at 150 and 250 Hz in order to minimize harmonics at these frequencies. The impact of the PCHC is shown in Figure 9a–d where grid current third order harmonic is reduced to 3.4% and 3.7% and the fifth order harmonic is reduced to 2.5% and 3% at the higher and lower power levels respectively. This result in a minimized grid current THD of 5.2% and 5.8% at both levels respectively. Hence, the effectiveness of the PCHC is verified experimentally. Bode plots of the conventional PR controller are shown in Figures 8e and 9e versus the bode plots of PR controller proposed in the experimentation, with its cascaded third and fifth-order harmonic compensator.

L_{dc} = 50 mH, **Conventional Proportional Resonant Controller (CPRC)**

25 ms/div, ch2:1 A/div

(**a**)

25 ms/div, ch2:1 A/div

(**b**)

Figure 8. *Cont.*

(c)

(d)

(e)

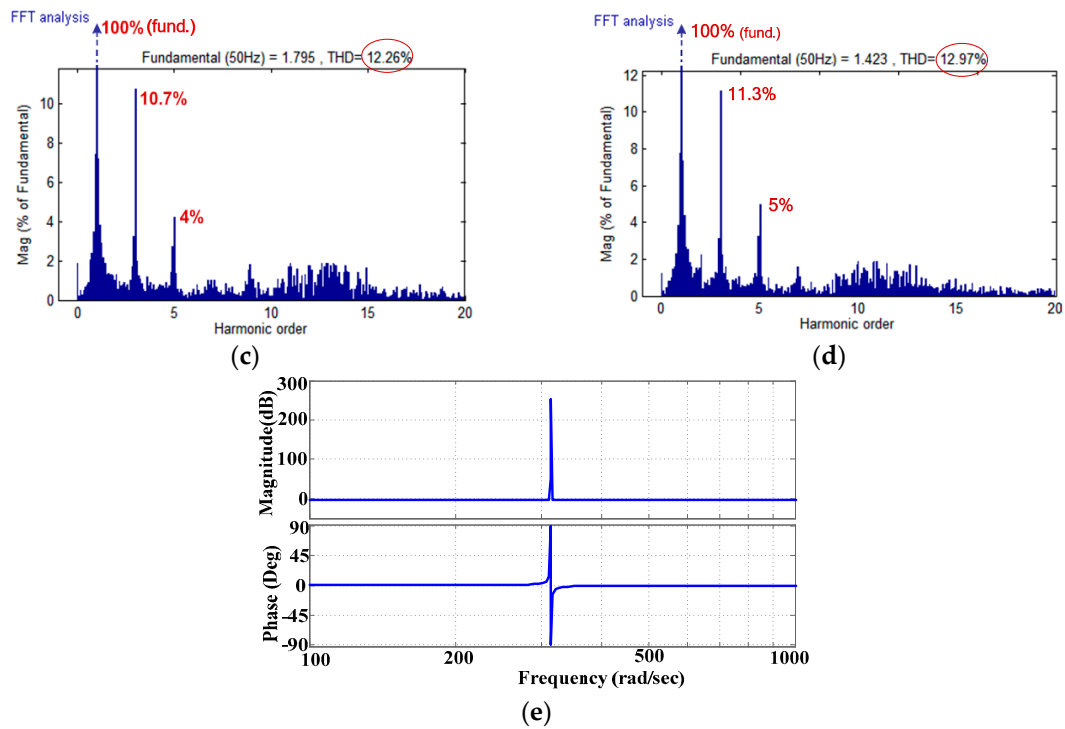**Figure 8.** Zoom into system performance applying CPRC; CSI grid current, and grid current with its fast Fourier transform (FFT) analysis at (**a**,**c**) high power level, and (**b**,**d**), low power level, and (**e**) Bode plot.

L_{dc} = 50 mH, Proposed Cascaded Harmonic Compensator (PCHC)

25 ms/div, ch2:1 A/div

(a)

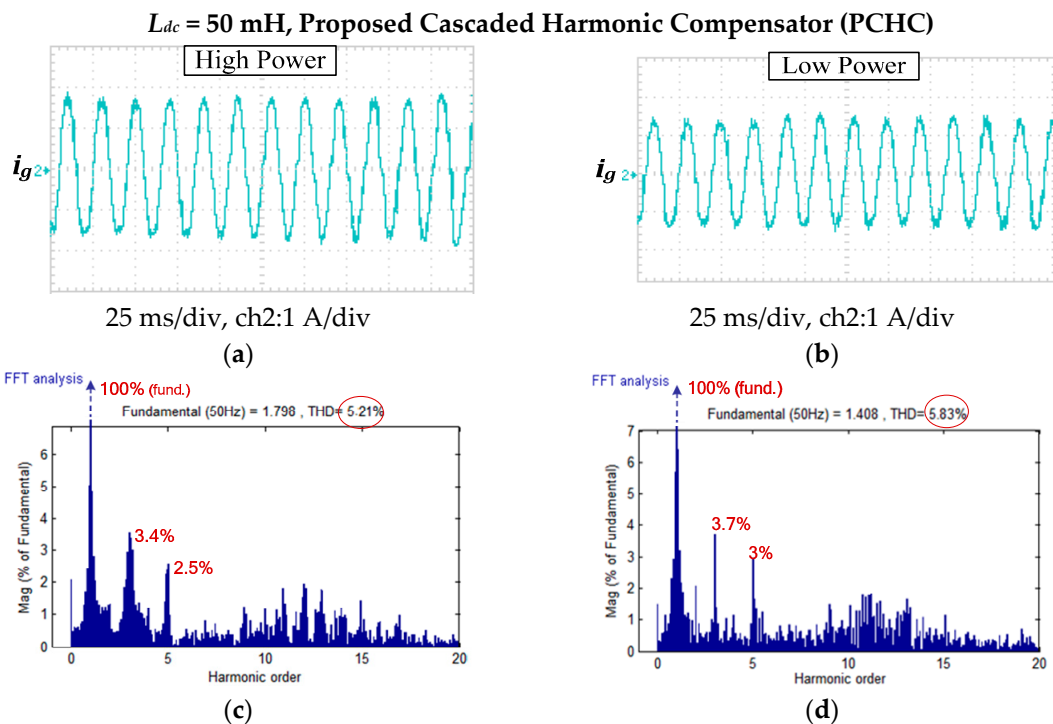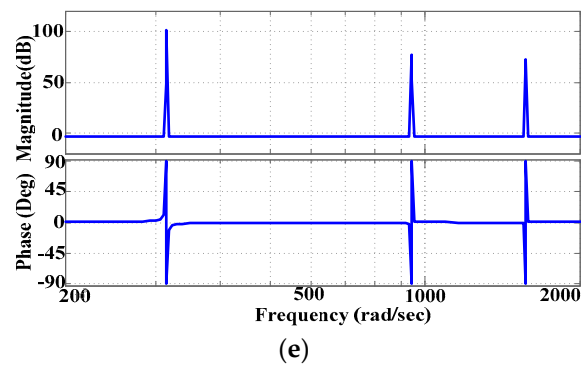25 ms/div, ch2:1 A/div

(b)

(c)

(d)

Figure 9. *Cont.*

(**e**)

Figure 9. Zoom into system performance applying PCHC; CSI grid current, and grid current with its FFT analysis at (**a**,**c**), high power level, and (**b**,**d**), low power level, and (**e**) Bode plot.

6. Conclusions

A modified cascaded proportional resonant controller, applied to single-phase single-stage PV grid connected CSI, is proposed. The presented controller succeeds in improving the CSI performance with the privilege of reducing the DC-link inductor compared to classical CSI controllers. Modeling and design of the single-phase single-stage grid-tied PV CSI is presented in this paper with its enhanced PWM switching technique associated with the proposed enhanced performance controller. The feasibility and effectiveness of the proposed cascaded PR controller have been established by simulation and experimentally as well. The obtained results reveal the superiority of the proposed controller which selectively eliminated the grid current low order harmonics using smaller value DC-link inductor when compared to the classical control technique. Consequently, system performance is enhanced under the proposed controller, leading to overall cost, size, and footprint reduction. Appendix B summarizes a detailed comparison between the proposed controller and the competitors listed in literature.

7. Discussion

In this subsection, the authors attempt to clarify several critical issues raised during the submission process. Those aspects, highlighted by the reviewers, focus mainly on helping the readers to easily understand the article and eliminate any misunderstanding/concerns that may arise. Among those issues:

1. How accurate is the Low-Budget PV Emulator and to What Extend its Characteristics Affect the Experimental Results?

For the simulation analysis: the authors utilize a detailed double-diode PV panel model with practical PV panel parameters embedded in the Simulink file. Hence, the simulation results are of very satisfactory level.

For the experimental investigation: the utilized low-cost emulator highly matches a corresponding PV panel as clarified from Figure 5b. Yet, the authors admit that a high-end Solar Array Simulator (SAS) (programmable switched mode DC power supply offering accurate PV characteristics) would reveal slightly different results specially when the operation travels from the constant-voltage to the constant-region and vice versa as the utilized low-cost emulator offers symmetrical inverted bell-shape characteristic while typical PV panel curve is steep. But, as the experimental illustrated results were utilized as a comparative analysis between the proposed controller and the classical one from the harmonic mitigation aspect, transient analysis would be of less importance in the current manuscript.

2. Comments on System Efficiency Results

Although CPRC and PCHC seem to achieve close performance, they differ in efficiency as well in harmonic cancellation which is tolerated to IEEE std [58–60].

Regarding system efficiency:

CSI DC/AC converters conversion efficiency ($\zeta_{\text{conv.}} = \frac{Output\ power\ to\ load}{Input\ DC\ power}$) is a critical issue to assess converter performance. However, for the converters under syudey, the input is usually a Renewable Energy source (RES) where the converter input voltage and current are utilized for maximum power tracking. This leads to RES current and voltage ripples and, in consequently, delivered power ripples which deteriorate the converter MPPT performance. Another efficiency aspect must be considered, usually of equal or even more importance than the converter power conversion efficiency, typically the converter tracking efficiency [60].

The converter overall efficiency accommodates both MPPT tracking efficiency and power conversion efficiency. The former ($\zeta_{\text{MPPT}} = \frac{RES\ tracked\ power}{Available\ maximum\ RES\ power\ at\ same\ conditions}$) decreases with the increase in the extracted RES power ripples and input converter current oscillations, driving converter to deliver less power. On the contrary, the converter power conversion efficiency ($\zeta_{\text{conv.}} = \frac{Output\ power\ to\ load}{RES\ tracked\ power}$) is the converter ability to deliver the RES tracked power to the load. This efficiency decreases with the increase in converter losses linearly proportional to large inductances with high copper losses [60].

On reviewing the efficiency results in Table 4, as the DC-link inductor decreased, it was expected that the efficiency decreased as well due to the expected increase in the power ripples, yet the contrary occurred for both CPRC ($\zeta_{\text{overall.}}$ increased from 86% to 92%) and PCHC (92%). This can be explained as the DC-link inductor value decreased, the conduction loss decreased as well, hence increasing the conversion efficiency while the tracking efficiency degraded due to the increase in the ripples. For overall system evaluation at this particular operating test conditions, the conversion efficiency was more dominant, hence the overall efficiency improved despite of the slight decrease in the tracking efficiency.

Table 4. Detailed efficiency assessment.

|	ζ_{OVERALL}	$\zeta_{\text{conv.}}$	$\zeta_{\text{MPPT.}}$
CPRC at 150 mH	86%	90%	95%
CPRC at 50 mH	92%	97%	94%
PCHC at 50 mH	92%	97%	94%

Regarding system harmonics:

The PCHC succeeded in mitigating more low-order harmonics than CPRC using the same DC-link inductor value and consequently achieve the best efficiency and lowest THD.

It's clear from Figure 10a,b that less ripples were encountered in the DC current (PV current) and in turn in the PV power in case of 150 mH which in turn increased the tracked PV power. However, increasing the DC link inductor increased the DC-link losses consequently resulting in less load power in case of 150 mH. Hence, the proposed techniques applying the 50 mH DC-link inductor achieved higher overall efficiency rather than when applying the 150 mH inductor in the DC-link.


(a)
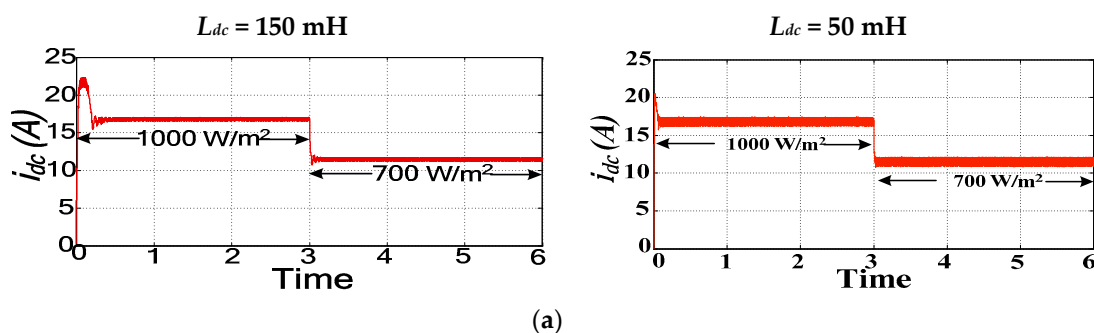
Figure 10. *Cont.*
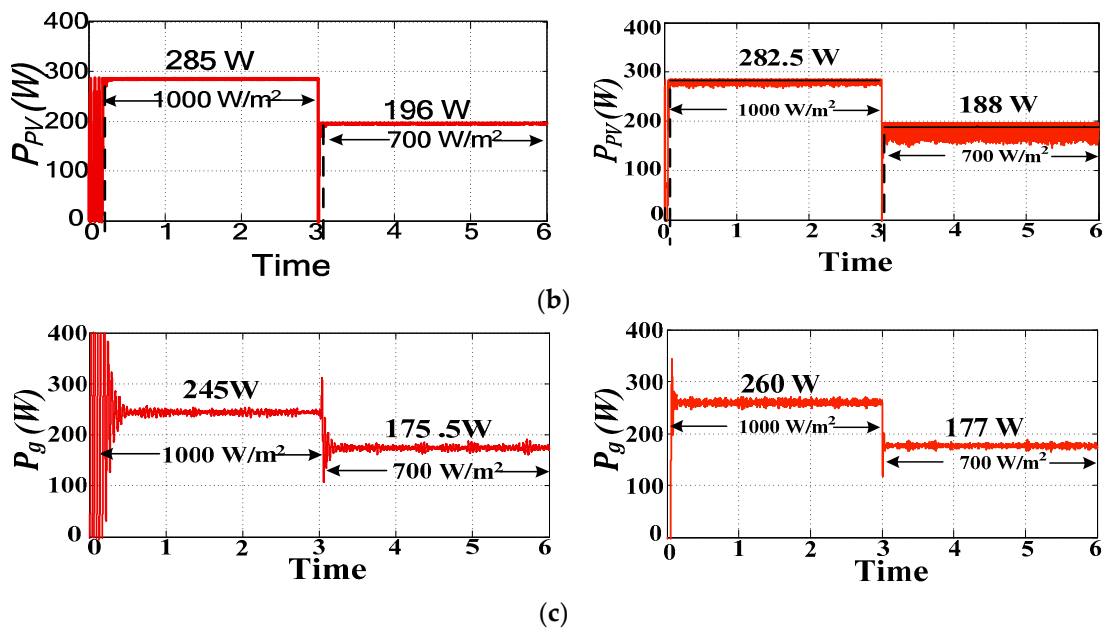
Figure 10. PCHC performance comparison when applying L_{dc} of 150 mH and 50 mH under irradiance variation: (**a**) DC-link current, (**b**) PV power, and (**c**) average grid power.

For more illustration, the PCHC is attested and compared at 2 DC-link inductor values as follows:

It's clear from Figure 11a,b that the proposed technique, applying both inductors' values, gave close satisfactory grid current response at both power levels (sinusoidal waveform with unity power factor and acceptable THD). However, the less DC-link inductor of 50 mH showed less losses achieving more grid current amplitude in turn more load power and higher efficiency. Although the 50 mH shows more grid current THD rather than that encountered in case of the 150 mH, the former still achieved current THD that complies with the IEEE 519 standards.
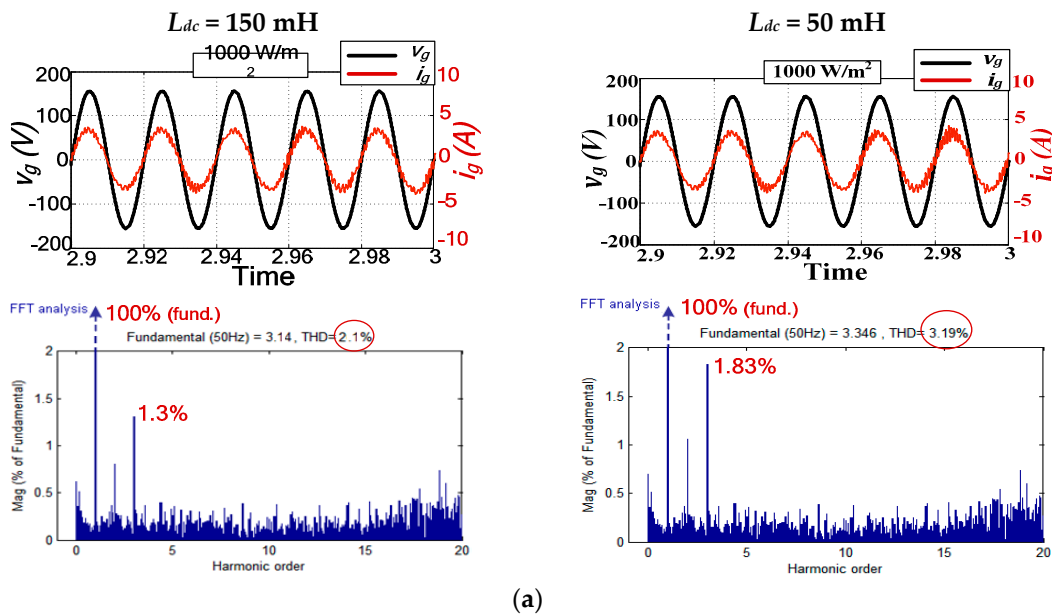
Figure 11. *Cont.*
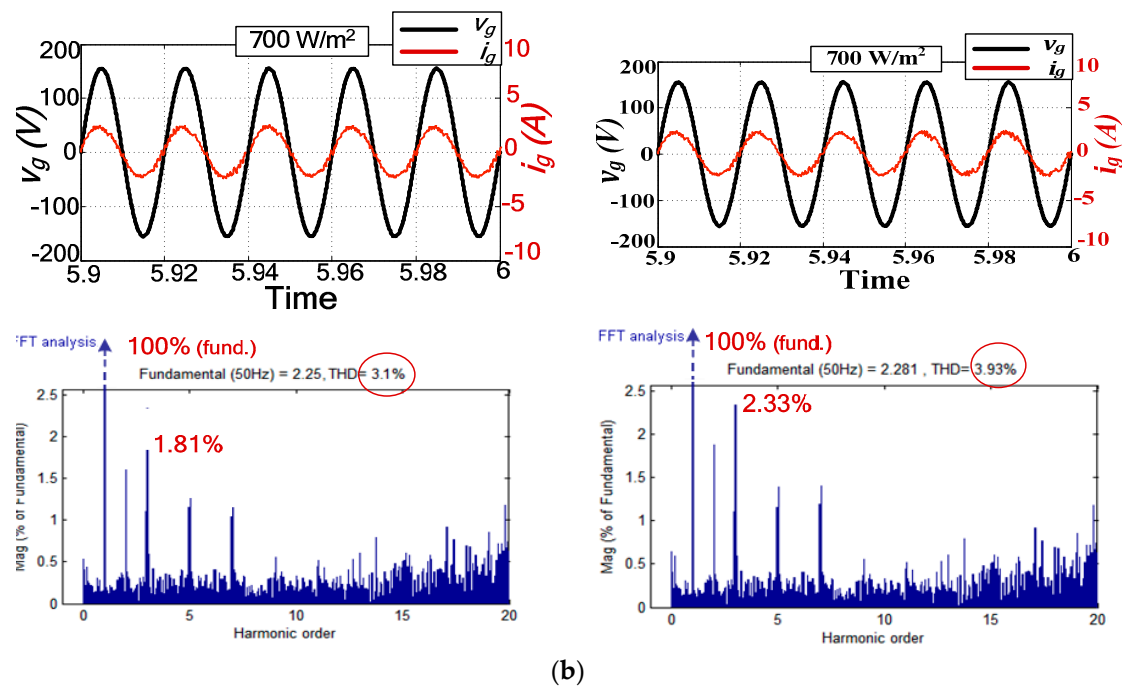
Figure 11. Zoom on PCHC grid current response when applying L_{dc} of 150 mH and 50 mH under irradiance variation: (**a**) high power level, (**b**) low power level.

In conclusion, Figures 10 and 11 show that applying the less DC-link inductor with the proposed technique resulted in higher overall efficiency and meanwhile satisfactory grid current response with acceptable THD.

3. Applicability of the Proposed Controller

The proposed cascaded harmonic compensator was manly applied to grid connected CSIs. As a competitor to VSIs [58,59], CSIs recently attracted a noticeable research interest to replace VSIs in various applications. Renewable energy utility interactive grid integration converters are the main application that CSI can replace VSI due to the previously discussed privileges of CSIs. Regarding the commercially available converters, CSIs are still in their infancy stage. Their market share is still very limited though promising due to the massive research recently published regarding efficiency improvement and performance enhancement. Several limitations are facing the utilization of CSI in medium-to-high power applications, mainly the dc-link inductor size and the power electronic switches' rating. Rockwell Automation® has recently launched the first ever medium voltage CSI as motor drive relying on novel water-cooled inductor and high-end insulated gate-commutated thyristors. The authors think that the development of silicon-carbide semiconductors and the research towards utilization of nano-crytalline cores would definitely contributes to increase CSI market share within the near future.

4. Point of Common Coupling Distortion

The assessment of any proposed controller/system must be performed at practical conditions. For grid connected renewable energy converters, point of common coupling (PCC) is a traditional low voltage distribution bus. The IEEE 519 std. limits the voltage harmonics of grid bus voltages to be under 8% for bus voltage under 1 kV [58].

Despite all the simulation results are performed under pure sinusoidal grid voltage as literature, the authors present a complete experimental validation for the proposed controller where all the experimental results are attested at typical near-sinusoidal grid voltage within the IEEE Std. with THD = 3.9% as illustrated in Figure 12. Therefore, the results presented in the submitted manuscript

investigate the proposed controller performance under ideal sinusoidal PCC (simulation results Figure 4) and practical grid voltage (experimental results Figures 6 and 7).

10 ms/div, ch1:200 V/div

(**a**)   (**b**)
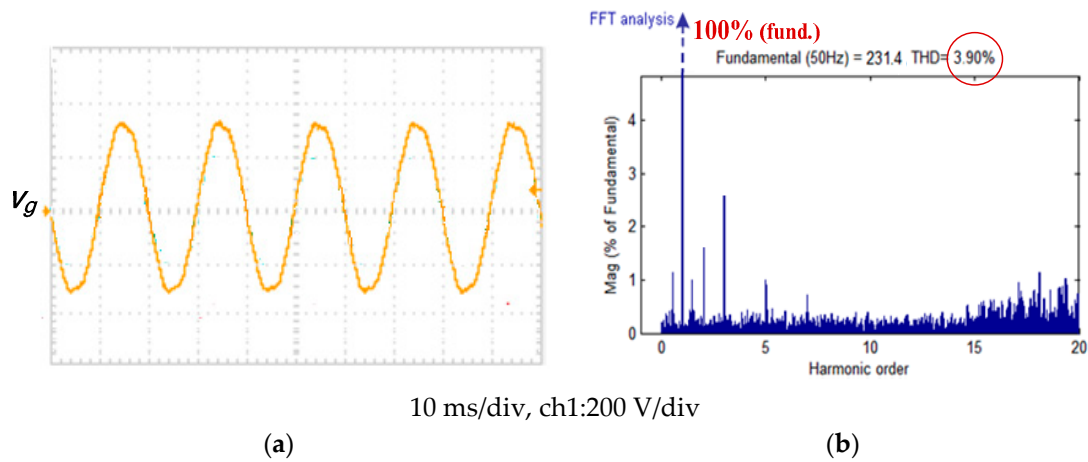
Figure 12. PCC grid voltage. (**a**) Grid voltage and (**b**) Grid current with its FFT analysis.

Conflicts of Interest: The authors declare no conflict of interest.
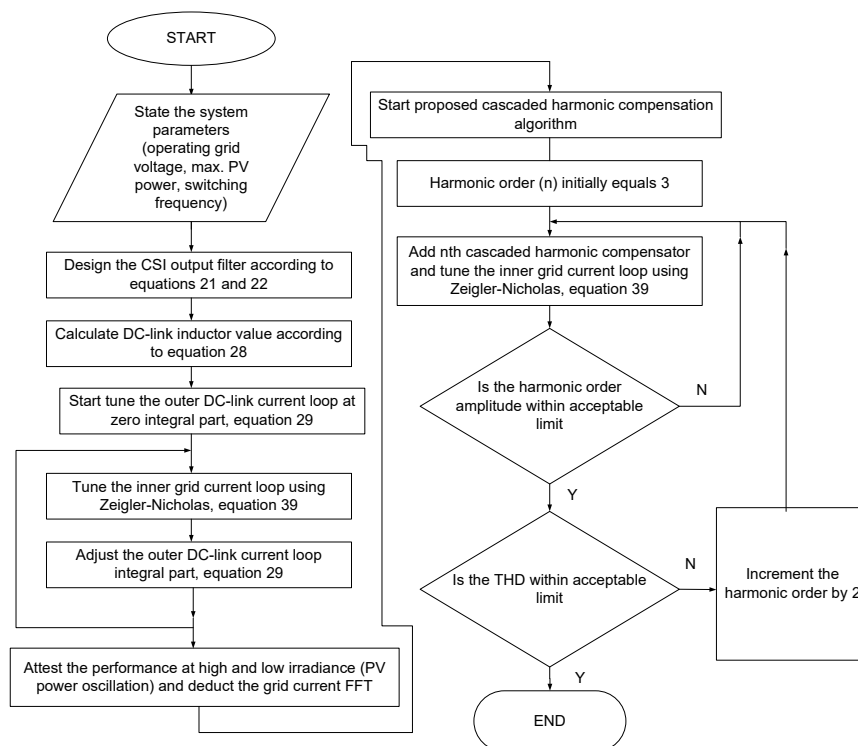
Appendix A

Figure A1. Step-by-step design guidance.

Appendix B

Table A1. Comparison table between the proposed controller and other competitors in literature.

Reference	Hardware	PWM Technique	Harmonic Mitigation Method	Experimental THD	Advantages	Disadvantages
[20]	Single phase	PAM	Using PWM only	No experimental results (4.8% in simulation)	1. Simplified PWM 2. No extra hardware	1. Limited performance at low modulation indices 2. Not harmonic specific cancellation
[21]	Single phase	NPWM	Using PWM only	4.42%		1. Analogue based 2. Deteriorated THD at low power operation
[25]	Single phase	SPWM	Using PWM only via 3rd harmonic cancellation	No experimental THD calculation (3.42% in simulation)		1. Only mitigates 3rd harmonic grid current.
[26]	Single phase	Modified carrier based	double-tuned parallel resonant circuit to attenuate the 2nd and 4th order harmonics at the inverter dc side	2.3%	1. Double action mitigation both hardware and software 2. High performance	1. High cost and size 2. Bulky 3. Difficult to tune the double parallel filter
[27]	Single phase	Pulse transform witching table	Active buffer power decoupling circuit	4.24%	1. High performance 2. High power density	1. More active semiconductors 2. High cost and size 3. bulky 4. Extra voltage sensor is needed
Proposed controller	Single phase	Modified sinusoidal	Software based Cascaded harmonic compensators for the grid current control	3.19%	1. High performance 2. Low cost and size 3. Less bulky 4. Easily tuned compensators	1. Care must be taken at various DC-link inductor values specially at very low modulation indices

Appendix C

Table A2. System parameters used in simulation analysis and experimental validation.

	Simulation Analysis Parameters	Experimental Validation Parameters
Grid voltage	220 V single phase pure sinusoidal supply	220 V single phase near-sinusoidal supply at IEEE519 Std. distortion level THD = 3.9%
Grid frequency	50 Hz	
Output filter Capacitance	25 μF	
Output filter Inductance	5 mH	
Switching frequency	15 KHz	
PV panel	285 W PV panel ASE-285-DGF/17 MODULE	Low-cost PV emulator

References

1. Guerrero, J.M.; Blaabjerg, F.; Zhelev, T.; Hemmes, K.; Monmasson, E.; Jemei, S.; Comech, M.P.; Granadino, R.; Frau, J.I. Distributed generation: Toward a new energy paradigm. *IEEE Ind. Electron. Mag.* **2010**, *4*, 52–64. [CrossRef]
2. Liserre, M.; Sauter, T.; Hung, J.Y. Future energy systems: Integrating renewable energy sources into the smart power grid through industrial electronics. *IEEE Ind. Electron. Mag.* **2010**, *4*, 18–37. [CrossRef]
3. Gonzalez, R.; Lopez, J.; Sanchis, P.; Marroyo, L. Transformerless inverter for single-phase photovoltaic systems. *IEEE Trans. Power Electron.* **2007**, *22*, 693–697. [CrossRef]
4. National Renewable Energy Laboratory (NREL). *Energy Analysis: Solar Power and the Electric Grid*; National Renewable Energy Laboratory: Golden, CO, USA, 2010.
5. Kouro, S.; Leon, J.I.; Vinnikov, D.; Franquelo, L.G. Grid-connected photovoltaic systems: An overview of recent research and emerging PV converter technology. *IEEE Ind. Electron. Mag.* **2015**, *9*, 47–61. [CrossRef]
6. Romero-Cadaval, E.; Francois, B.; Malinowski, M.; Qing-Chang, Z. Grid-connected photovoltaic plants: An alternative energy source, replacing conventional sources. *IEEE Ind. Electron. Mag.* **2015**, *9*, 18–32. [CrossRef]
7. Kjaer, S.B.; Pedersen, J.K.; Blaabjerg, F. A review of single-phase grid-connected inverters for photovoltaic modules. *IEEE Trans. Ind. Appl.* **2005**, *41*, 1292–1306. [CrossRef]
8. Romero-Cadaval, E.; Spagnuolo, G.; Franquelo, L.G.; Ramos-Paja, C.A.; Suntio, T.; Xiao, W.M. Grid-connected photovoltaic generation plants: Components and operation. *IEEE Ind. Electron. Mag.* **2013**, *7*, 6–20. [CrossRef]
9. Xiao, W.; Ozog, N.; Dunford, W. Topology study of photovoltaic interface for maximum power point tracking. *IEEE Trans. Ind. Electron.* **2007**, *54*, 1696–1704. [CrossRef]
10. Roman, E.; Alonso, R.; Ibanez, P.; Elorduizapatarietxe, S.; Goitia, D. Intelligent PV module for grid-connected PV systems. *IEEE Trans. Ind. Electron.* **2006**, *53*, 1066–1073. [CrossRef]
11. Chowdhury, S.; Chowdhury, S.P.; Crossley, P. *Microgrids and Active Distribution Networks*; IET Renewable Energy Series 6; Institution of Engineering and Technology: London, UK, 2009.
12. Blaabjerg, F.; Teodorescu, R.; Liserre, M.; Timbus, A.V. Overview of control and grid synchronization for distributed power generation systems. *IEEE Trans. Ind. Electron.* **2006**, *53*, 1398–1409. [CrossRef]
13. Eltawil, M.A.; Zhao, Z. Grid-connected photovoltaic power systems: Technical and potential problems—A review. *Renew. Sustain. Energy Rev.* **2010**, *14*, 112–129. [CrossRef]
14. Shimizu, T.; Wada, K.; Nakamura, N. Flyback-type single-phase utility interactive inverter with power pulsation decoupling on the dc input for an ac photovoltaic module system. *IEEE Trans. Power Electron.* **2006**, *21*, 1264–1272. [CrossRef]
15. Hu, H.; Harb, S.; Kutkut, N.; Batarseh, I.; Shen, Z.J. A review of power decoupling techniques for micro inverters with three different decoupling capacitor locations in PV systems. *IEEE Trans. Power Electron.* **2013**, *28*, 2711–2726. [CrossRef]
16. Jain, S.; Agarwal, V. A single-stage grid connected inverter topology for solar PV systems with maximum power point tracking. *IEEE Trans. Power Electron.* **2007**, *22*, 1928–1940. [CrossRef]

17. Wu, T.; Chang, C.; Lin, L.; Kuo, C. Power loss comparison of single- and two-stage grid-connected photovoltaic systems. *IEEE Trans. Energy Convers.* **2011**, *26*, 707–715. [CrossRef]

18. Jain, S.; Agarwal, V. Comparison of the performance of maximum power point tracking schemes applied to single-stage grid-connected photovoltaic systems. *IET Electr. Power Appl.* **2007**, *1*, 753–762. [CrossRef]

19. Chen, Y.M.; Chang, C.H.; Wu, H.C. DC-Link capacitor selections for the single-phase grid-connected PV system. In Proceedings of the 2009 International Conference on Power Electronics and Drive Systems (PEDS), Taipei, Taiwan, 2–5 November 2009; pp. 72–77.

20. Hirachi, K.; Ishitobi, M.; Matsumoto, K.; Hatton, H.; Ishibashi, M.; Nakaoka, M.; Takahashi, N.; Kato, Y. Pulse area modulation control implementation for single-phase current source-fed inverter for solar photovoltaic power conditioner. In Proceedings of the IEEE Power Electronic Drives and Energy Systems for Industrial Growth Conference, Perth, Australia, 1–3 December 1998; pp. 677–682.

21. Li, R.T.H.; Chung, H.S.H.; Chan, T.K.M. An active modulation technique for single-phase grid-connected CSI. *IEEE Trans. Power Electron.* **2007**, *22*, 1373–1382. [CrossRef]

22. Patel, H.; Agarwal, V. A Single-Stage Single-Phase Transformer-Less Doubly Grounded Grid-Connected PV Interface. *IEEE Trans. Energy Convers.* **2009**, *24*, 93–101. [CrossRef]

23. Ertasgin, G.; Whaley, D.M.; Ertugrul, N.; Soong, W.L. Analysis and design of energy storage for current-source 1-ph grid-connected PV inverters. In Proceedings of the IEEE Applied Power Electronics Conference and Exposition (APEC 2008), Austin, TX, USA, 24–28 February 2008; pp. 1229–1234.

24. Komurcugil, H. Steady-state analysis and passivity-based control of single-phase PWM current-source inverters. *IEEE Trans. Ind. Electron.* **2010**, *57*, 1026–1030. [CrossRef]

25. Darwish, A.; Abdelsalam, A.K.; Massoud, A.M.; Ahmed, S. Single phase grid connected current source inverter: Mitigation of oscillating power effect on the grid current. In Proceedings of the IET Conference on Renewable Power Generation, Edinburgh, UK, 6–8 September 2011; pp. 1–7.

26. Alajmi, B.N.; Ahmed, K.H.; Adam, G.P.; Williams, B.W. Single-phase single-stage transformer less grid-connected PV system. *IEEE Trans. Power Electron.* **2013**, *28*, 2664–2676. [CrossRef]

27. Ohnuma, Y.; Orikawa, K.; Itoh, J. A single-phase current-source PV inverter with power decoupling capability using an active buffer. *IEEE Trans. Ind. Appl.* **2015**, *51*, 531–538. [CrossRef]

28. Wu, B. *High-Power Converters and AC Drives Handbook*; John Wiley & Sons, Inc.: Hoboken, NJ, USA, 2006.

29. Wiechmann, E.P.; Aqueveque, P.; Burgos, R.; Rodríguez, J. On the efficiency of voltage source and current source inverters for high-power drives. *IEEE Trans. Ind. Electron.* **2008**, *55*, 1771–1782. [CrossRef]

30. Abdelsalam, A.K.; Massoud, A.; Darwish, A.; Ahmed, S. Simplified generic on-line PWM technique for single phase grid connected current source inverters. In Proceedings of the IEEE Applied Power Electronics Conference and Exposition (APEC 2012), Orlando, FL, USA, 5–9 February 2012; pp. 1398–1403.

31. Rashid, M.H. *Power Electronics Handbook*; Butterworth-Hinemann: Oxford, UK, 2011.

32. Araújo, S.V.; Zacharias, P.; Mallwitz, R. Highly efficient single-phase transformerless inverters for grid-connected photovoltaic systems. *IEEE Trans. Ind. Electron.* **2010**, *57*, 3118–3128. [CrossRef]

33. Hohm, D.P.; Ropp, M.E. Comparative study of maximum power point tracking algorithms. *Prog. Photovolt. Res. Appl.* **2003**, *11*, 47–62. [CrossRef]

34. Esram, T.; Chapman, P.L. Comparison of photovoltaic array maximum power point tracking techniques. *IEEE Trans. Energy Convers.* **2007**, *22*, 439–449. [CrossRef]

35. Spiazzi, G.; Buso, S.; Mattavelli, P.; Tenti, P. Low complexity MPPT techniques for PV module converters. In Proceedings of the International Power Electronics Conference, Sapporo, Japan, 21–24 June 2010; pp. 2074–2081.

36. Liu, F.; Duan, S.; Liu, F.; Liu, B.; Kang, Y. A variable step size INC MPPT method for PV systems. *IEEE Trans. Ind. Electron.* **2008**, *55*, 2622–2628.

37. Mei, Q.; Shan, M.; Liu, L.; Guerrero, J.M. A novel improved variable step-size incremental- resistance MPPT method for PV systems. *IEEE Trans. Ind. Electron.* **2011**, *58*, 2427–2434. [CrossRef]

38. Zakzouk, N.E.; Abdelsalam, A.K.; Helal, A.A.; Williams, B.W. Modified variable-step incremental conductance maximum power point tracking technique for photovoltaic systems. In Proceedings of the IEEE Industrial Electronics Society Conference (IECON 2013), Vienna, Austria, 10–13 November 2013; pp. 1741–1748.

39. Ninad, N.A.; Lopes, L.A.C. Operation of single-phase grid-connected inverters with large DC bus voltage ripple. In Proceedings of the IEEE Electrical Power Conference (EPC 2007), Montreal, QC, Canada, 25–26 October 2007; pp. 172–176.

40. Wai, R.J.; Wang, W.H. Grid-connected photovoltaic generation system. *IEEE Trans. Circuits Syst.* **2008**, *55*, 953–964.

41. Ciobotaru, M.; Teodorescu, R.; Blaabjerg, F. Control of single-stage single-phase PV inverter. In Proceedings of the IEEE European Power Electronics and Applications Conference (EPE), Dresden, Germany, 11–14 September 2005; pp. 1–10.

42. Zammit, D.; Staines, C.S.; Apap, M. Comparison between PI and PR current controllers in grid connected PV inverters. *Int. J. Electr. Robot. Electron. Commun. Eng.* **2014**, *8*, 217–222.

43. Fukuda, S.; Yoda, T. A novel current-tracking method for active filters based on a sinusoidal internal model. *IEEE Trans. Ind. Electron.* **2001**, *37*, 888–895. [CrossRef]

44. Yuan, X.; Merk, W.; Stemmler, H.; Allmeling, J. Stationary-frame generalized integrators for current control of active power filters with zero steady-state error for current harmonics of concern under unbalanced and distorted operating conditions. *IEEE Trans. Ind. Appl.* **2002**, *38*, 523–532. [CrossRef]

45. Mastromauro, R.A.; Liserre, M.; Aquila, A.D. Control issues in single-stage photovoltaic systems: MPPT, current and voltage control. *IEEE Trans. Ind. Inform.* **2012**, *8*, 241–254. [CrossRef]

46. Teodorescu, R.; Blaabjerg, F.; Liserre, M.; Loh, P.C. Proportional-resonant controllers and filters for grid connected voltage-source converters. *IEE Proc. Electr. Power Appl.* **2006**, *153*, 750–762. [CrossRef]

47. Kulkarni, A.; John, V. Mitigation of lower order harmonics in a grid-connected single-phase PV inverter. *IEEE Trans. Power Electron.* **2013**, *28*, 5024–5037. [CrossRef]

48. Chattopadhyay, R.; De, A.; Bhattacharya, S. Comparison of PR controller and damped PR controller for grid current control of LCL filter based grid-tied inverter under frequency variation and grid distortion. In Proceedings of the IEEE Energy Conversion Congress and Exposition (ECCE), Pittsburgh, PA, USA, 14–18 September 2014; pp. 3634–3641.

49. Castilla, M.; Miret, J.; Matas, J.; de Vicuña, L.G.; Guerrero, J.M. Control design guidelines for single-phase grid-connected photovoltaic inverters with damped resonant harmonic compensators. *IEEE Trans. Ind. Electron.* **2009**, *56*, 4492–4501. [CrossRef]

50. Castilla, M.; Miret, J.; Camacho, A.; Matas, J.; de Vicuña, L.G. Reduction of current harmonic distortion in three-phase grid-connected photovoltaic inverters via resonant current control. *IEEE Trans. Ind. Electron.* **2013**, *60*, 1464–1471. [CrossRef]

51. Teodorescu, R.; Blaabjerg, F. Proportional-resonant controllers. A new breed of controllers suitable for grid-connected voltage-source converters. *Proc. Optim.* **2004**, *3*, 9–14.

52. de Araujo, M.B.; Rocha, L.R.; Martins, L.T.; Vieira, R.P. Multiloop Current Control Strategy for a Grid-connected VSI with LCL Filter Using Backstepping and Proportional+Resonant Controller. In Proceedings of the 2019 IEEE PES Innovative Smart Grid Technologies Conference, Gramado, Brazil, 15–18 September 2019; pp. 1–6.

53. Teodorescu, R.; Blaabjerg, F.; Borup, U.; Liserre, M. A new control structure for grid-connected LCL PV inverters with zero steady-state error and selective harmonic compensation. In Proceedings of the IEEE Applied Power Electronics Conference and Exposition (APEC 2004), Anaheim, CA, USA, 22–26 February 2004; pp. 580–589.

54. Ciobotaru, M.; Kerekes, T.; Teodorescu, R.; Bouscayrol, A. PV inverter simulation using MATLAB/Simulink graphical environment and PLECS blockset. In Proceedings of the IEEE Industrial Electronics Conference (IECON2006), Paris, France, 6–10 November 2006; pp. 5313–5318.

55. Timbus, A.; Liserre, M.; Teodorescu, R.; Rodriguez, P.; Blaabjerg, F. Evaluation of current controllers for distributed power generation systems. *IEEE Trans. Power Electron.* **2009**, *24*, 654–662. [CrossRef]

56. IEEE. *IEEE Recommended Practice and Requirements for Harmonic Control in Electric Power Systems*; IEEE: New York, NY, USA, 1993.

57. Mukerjee, A.K.; Dasgupta, N. DC power supply used as photovoltaic simulator for testing MPPT algorithms. *Renew. Energy* **2006**, *32*, 587–592. [CrossRef]

58. IEEE. *IEEE Recommended Practice and Requirements for Harmonic Control in Electric Power Systems*; IEEE: New York, NY, USA, 2014.

59.   Zakzouk, N.E.; Abdelsalam, A.K.; Helal, A.A.; Williams, B.W. PV single-phase grid-connected converter: DC-link voltage sensorless prospective. *IEEE J. Emerg. Sel. Top. Power Electron.* **2017**, *5*, 526–546. [CrossRef]
60.   Zakzouk, N.E.; Khamis, A.K.; Abdelsalam, A.K.; Williams, B.W. Continuous-input continuous-output current buck-boost DC/DC converters for renewable energy applications: Modelling and performance assessment. *Energies* **2019**, *12*, 2208. [CrossRef]